Examination of Coupling between an Upper-Tropospheric Cloud System and Synoptic-Scale Dynamics Diagnosed from Wind Profiler and Radiosonde Data

GERALD G. MACE

Department of Meteorology, The Pennsylvania State University, University Park, Pennsylvania

DAVID O'C. STARR

Laboratory for Atmospheres, NASA/Goddard Space Flight Center, Greenbelt, Maryland

THOMAS P. ACKERMAN

Department of Meteorology, The Pennsylvania State University, University Park, Pennsylvania

PATRICK MINNIS

Atmospheric Sciences Division, NASA/Langley Research Center, Hampton, Virginia

(Manuscript received 19 July 1994, in final form 15 December 1994)

ABSTRACT

The evolution of synoptic-scale dynamics associated with a middle and upper tropospheric cloud event that occurred on 26 November 1991 is examined. The case under consideration occurred during the FIRE Cirrus-II Intensive Field Observing Period held in Coffeyville, Kansas, during November–December 1991. Using data from the wind profiler demonstration network and a temporally and spatially augmented radiosonde array, emphasis is given to explaining the evolution of the kinematically derived ageostrophic vertical circulations and correlating the circulation with the forcing of an extensively sampled cloud field. This is facilitated by decomposing the horizontal divergence into its component parts through a natural coordinate representation of the flow. Ageostrophic vertical circulations are inferred and compared to the circulation forcing arising from geostrophic confluence and shearing deformation derived from the Sawyer–Eliassen equation. It is found that a thermodynamically indirect vertical circulation existed in association with a jet streak exit region. The circulation was displaced to the cyclonic side of the jet axis due to the orientation of the jet exit between a deepening diffluent trough and a building ridge. The cloud line formed in the ascending branch of the vertical circulation, with the most concentrated cloud development occurring in conjunction with the maximum large-scale vertical motion. The relationship between the large-scale dynamics and the parameterization of middle and upper tropospheric clouds in large-scale models is discussed, and an example of ice water contents derived from a parameterization forced by the diagnosed vertical motions and observed water vapor contents is presented.

1. Introduction

In his review article, Liou (1986) states that cirrus clouds are one of the most important yet least understood components of the climate system. Covering as much as one-third of the earth's surface and having unique microphysical and radiative characteristics, cirrus undoubtedly has a profound influence on climate. The ability to characterize accurately these upper-tropospheric ice phase clouds in general circulation models has long been recognized as a serious shortcoming of present-day simulations of future and past climate. Cirrus clouds present a multifaceted challenge that spans the entire range of the cloud parameterization problem. At the smallest scales, the optical characteristics of cirrus that stem, in large part, from complicated crystal characteristics are not well-known and, therefore, are difficult to accurately represent in a GCM parameterization. At smaller scales, cirrus clouds owe their existence primarily to turbulent motions. However, as shown in the modeling studies of Starr and Cox (1985a,b), the meso- to synoptic-scale ascent is quite important to the evolution of the macroscopic cloud properties. Macroscopic characteristics such as cloud thickness, aerial coverage, and optical depth have been shown to be quite sensitive to the large-scale vertical motion. This sensitivity to the large-scale ascent con-

Corresponding author address: Dr. Gerald G. Mace, Department of Meteorology, College of Earth and Mineral Sciences, The Pennsylvania State University, 503 Walker Building, University Park, PA 16802-5013.

tributes to the mesoscale organization of cirrus cloud systems documented in several case studies (Sassen et al. 1989; Starr and Wylie 1990).

That cirrus cloud systems tend to be organized on scales approaching that of current GCMs makes realistic parameterization of cirrus an achievable goal. This presumes that relationships between the model dynamics and thermodynamics and the occurrence and characteristics of nonconvective cirrus cloud are well understood. This is not, however, the case. Most GCMs diagnose the presence of supersaturation clouds in the upper troposphere based on undocumented relationships between cirrus occurrence and relative humidity (Slingo 1987). The optical properties are, then, specified based on cloud height. While the humidity undoubtedly plays a crucial role in the existence of cirrus clouds, well-established statistical relationships between upper-tropospheric relative humidity on any scale and the resulting cloud fraction, cloud depth, or optical characteristics do not as yet exist. This is largely due to the difficulty of accurately measuring water vapor content at cold upper-tropospheric temperatures (Starr and Melfi 1991). As pointed out by Slingo (1987), several additional parameters may be useful in leading to correct diagnoses of the presence of cloud. These are the vertical velocity, stability, and vertical wind shear. Considering the coarse vertical resolution of most GCMs relative to the observed scales of many cirrus layers (Starr and Wylie 1990), Richardson number considerations would not be useful as a diagnostic since they ultimately depend on the depth over which the vertical finite differencing is conducted. This was shown in a radiosonde study by Starr and Cox (1980) where Richardson numbers computed using coarse vertical resolution were found to be poor predictors of the presence of cirrus. The vertical resolution of the soundings they used was only slightly finer than most GCMs.

An example of a physically based parameterization that uses the large-scale vertical velocity and the observed relative humidity is the ice water content parameterization described by Heymsfield and Donner (1990, hereafter referred to as the HD parameterization). This parameterization uses an expression that balances crystal sedimentation with vapor deposition. Ultimately, it is the large-scale vertical velocity and the water vapor availability that determine the quantity of ice in a particular layer. Essentially, the HD parameterization is a diagnostic synthesis of the physics used in the cirrus model of Starr and Cox (1985a).

In a recent study, Soden and Donner (1994), using ECMWF analyses and ISCCP cloud products, demonstrated that the HD parameterization is able to capture the spatial variability of optical depth on global scales. However, they noted large discrepancies between the absolute values of the parameterized and satellite-derived optical depths. While several factors may have contributed to the differences, the largely unknown relationship between large-scale vertical velocity and cirrus microphysical characteristics certainly contributed. This is evidenced by a strong latitudinal dependence of the discrepancies in their July study, the largest differences occurring in the Southern Hemisphere. While model error may have been a factor in the data-sparse Southern Hemisphere, it is equally likely that the cirrus formed in the baroclinic regions of the austral winter was fundamentally different from the cirrus formed in the more convectively active Tropics and summer hemisphere. The relationship between the bulk optical characteristics of cirrus and the synoptic regime in which they form is not presently understood. This lack of knowledge represents a fundamental deficiency in our ability to characterize accurately cloud–climate interaction in GCMs.

An improved understanding of the instantaneous radiative transfer through observed cirrus will not benefit climate prediction efforts unless a concomitant connection is achieved unambiguously between the clouds being studied and the actual dynamics on multiple scales. Furthermore, even though a correct diagnosis of the large-scale ascent and upper-tropospheric humidities is crucial, simply knowing these quantities is insufficient. The radiative characteristics of cirrus in a particular situation are undoubtedly a reflection of the history of the air mass in which they have formed (Sassen et al. 1994). The evolution of the vertical motions and the upper-tropospheric water vapor fields must be placed into the context of the evolving dynamics. In short, to advance toward the stated goals of the First ISCCP Regional Experiment (FIRE Project Office 1991), it is requisite upon us to quantitatively connect the observed radiative transfer and microphysics to a thorough and verifiable explanation of the observed GCM-resolvable large-scale dynamics.

The association of cirrus with midlatitude synoptic regimes has a long history in the literature (Stone 1957; Conover 1960). Heymsfield (1977) presented a detailed aircraft-based study of cirrus formation in a spectrum of midlatitude synoptic situations. Shapiro (1981) suggested using satellite-observed cirriform cellular structure as a means of diagnosing the turbulent scales associated with certain jet flows. Sassen et al. (1989), using lidar and radiosonde data, correlated the occurrence of cirrus with subtropical jet streams and elevated frontal zones. Using radiosonde network analyses and surface-based lidar and aircraft observations, Starr and Wylie (1990) analyzed several cirrus events associated with the passage of a jet streak and upper-tropospheric ridge. They found strong evidence for mesoscale organization of the cloud decks and noted that the cirrus formed in association with lower-tropospheric weather systems, although this association was due to a natural superposition of separate forcings rather than a common cause. They demonstrated that large-scale vertical motions in cirrus generating regions tended to be about 5–7 cm s^{-1}, but unambiguous estimates of the large-scale ascent could not be made in all cases.

In explaining the meso- and larger-scale dynamics of the cirrus events presented below, we will couch the explanation in terms of vertical circulations forced in jet flows (Keyser and Shapiro 1986). In a straight jet streak with negligible thermal advection, transverse ageostrophic motions associated with alongstream parcel accelerations lead to thermodynamically direct (indirect) vertical circulations in the jet entrance (exit) region. The vertical branches of these cells tend to straddle the jet axis with the relative magnitudes of the vertical and horizontal branches proportional to the potential vorticity, as can be seen by examining the Sawyer–Eliassen equation (Keyser and Shapiro 1986). More generally, the thermal advection cannot be neglected owing to the phase lags between the thermal and momentum fields. Therefore, cold (warm) air advection is typically found in the entrance (exit) region. The combined effect of thermal advection and horizontal shear tend to shift the vertical circulations laterally. For instance, cold air advection in the entrance region of a jet streak tends to shift the transverse ageostrophic circulation to the anticyclonic side of the jet axis. The placement of the descending branch beneath the jet axis in the entrance region occurs in association with elevated frontal zones and tropopause folds (Keyser and Shapiro 1986). Arguing from gradient wind concepts, Keyser and Shapiro (1986) conjectured that when a jet is placed at the base of a long-wave trough the alongstream ageostrophic motions induced by flow curvature will reinforce the vertical branches of the ageostrophic motions. It is the modulation of the ascending branches of the ageostrophic circulations by the flow field dynamics and their superposition with the upper-tropospheric moisture field that are of direct importance to the development and maintenance of many midlatitude cirrus cloud decks. For instance, Sassen et al. (1994) describe several cirrus events that displayed unusual microphysical and optical characteristics. It was shown that the characteristics of these clouds came about through a complicated history of tropopause folds associated with polar and subtropical jet streaks. Stratospheric aerosol injected into the upper troposphere interacted with subtropical moisture layers in the jet entrance regions to form these clouds. The dynamical history of the air mass was all-important to the resulting cirrus cloud characteristics.

Placing cloud evolution into a dynamical context can be accomplished quite efficiently using cloud-resolving mesoscale models. However, in such studies it is difficult to attribute discrepancies between observation and model output to the simulated dynamics or the cloud modeling algorithm. In order to compliment the mesoscale modeling efforts, we have implemented an analysis scheme based exclusively on combined wind profiler and radiosonde data. While a measure of uncertainty exists in the data, this uncertainty is generally quantifiable and places known bounds on the objectively analyzed quantities. The resulting description of the synoptic-scale dynamics represents a ground truth against which finer-scale models can be compared.

While the dynamical characteristics of elevated jet streaks have been discussed theoretically and diagnosed in the output of idealized models, few studies have used observations. A notable exception is the work of Shapiro (1981), who solved the Sawyer–Eliassen equation with the forcing defined via analysis of radiosonde and aircraft data. He demonstrated that horizontal shear of the geostrophic wind in the cross-stream direction acting on alongfront thermal gradients can force midtropospheric subsident motions. The front examined by Shapiro displayed a direct vertical circulation in the lower troposphere, while an indirect circulation was diagnosed in the upper troposphere. More recently, Sanders et al. (1991) examined an intense northwesterly jet and investigated the evolution of the potential vorticity field and strong subsidence beneath the jet core forced by cold air advection. Cammas and Ramond (1989) used ECMWF analyses to decompose the horizontal divergence and ageostrophic wind in a natural coordinate reference frame to show that the association of flow curvature with alongstream speed accelerations can significantly modify the classical models derived from the Sawyer–Eliassen equation and gradient wind concepts.

We will adopt the conceptual approach of Cammas and Ramond (1989) in this study. Working from objectively analyzed wind profiler and radiosonde data, the transverse ageostrophic circulation and its associated forcing will be estimated. The vertical circulations will be combined with analyses of the thermodynamic and water vapor structure in the upper troposphere to describe the evolution of a middle and upper tropospheric cloud field sampled during the FIRE Cirrus-II field campaign. The diagnosed dynamics and thermodynamics will be combined with the water vapor field in the HD parameterization to demonstrate the advantage of using data-based techniques to evaluate and improve cloud parameterizations.

2. Data processing and analysis techniques

The goal of the analysis presented herein is to document the evolution of the synoptic-scale dynamical mechanisms important to regional cloud formation. Given typical spacing between observing points of 175–200 km, the characteristics of the synoptic-scale dynamics are well resolved. While the dynamics on the mesoscale can be inferred from the data in certain cases, the spacing between data points precludes a quantitative analysis of the spatial characteristics of the meso- and smaller-scale features. Therefore, the data processing and analysis techniques described below are specifically designed to remove atmospheric signal below the spatial resolution of the network.

a. Initial processing of wind profiler data

The diagnostic analyses presented below rely exclusively on data collected from the Wind Profiler Demonstration Network (WPDN, Chadwick 1986) and the spatially and temporally augmented conventional radiosonde network. Figure 1 shows the geographic distribution of the radiosonde network and WPDN as it existed in November 1991. The WPDN, then composed of 18 profilers, existed in a swath roughly 350 km wide from southeast Wyoming to northern Louisiana. We will refer to the hexagonal array of wind profilers centered on the Lamont, Oklahoma (LMN), profiler as the inner array of the WPDN. Coffeyville, Kansas, the operational hub of the FIRE Cirrus-II IFO, is located at the northeast vertex of the inner array approximately 30 km south of the Neodesha, Kansas (NDS) profiler. Note that a special network of four cross-chain linked atmospheric sounding systems (CLASS) was situated such that Coffeyville was centered on the eastern side of an approximately equilateral triangle. The location of an array of National Weather Service radiosonde stations that conducted three hourly soundings during the case study period are also shown in Fig. 1.

The WPDN wind profilers, which operate at a frequency of 404.37 MHz and a wavelength of 74 cm, provide two modes of data sampling: a high mode and a low mode. The low mode is designed to sample the lower troposphere and provides measurements from 500 m AGL to 9.25 km AGL. The vertical resolution in this mode is 250 m with 250-m gate spacing. The high mode provides measurements from 7.5 to 16.25 km AGL at 1-km vertical resolution. Shorter pulse widths are used in the low mode and enable a higher vertical resolution. However, low signal to noise frequently becomes a problem for this mode above approximately 5–6 km. Therefore, the high-mode observations are used where the modes overlap, sacrificing vertical resolution for better overall data quality in the middle troposphere. For further details concerning wind profiler technology, the reader is referred to Gage and Balsley (1978). The wind profiler data used in this study are hourly averaged horizontal winds derived from the 6-minute averaged radial velocity statistics (Doppler moments). As described in detail by Mace (1994), a consensus averaging scheme (Strauch et al. 1981; Fischler and Bolles 1981) was applied to remove erroneous observations from the Doppler moments time series. After converting the oblique beam radial velocities to horizontal eastward and northward components, a running hourly average, centered on the nominal observation time, was applied to the horizontal components creating hourly mean horizontal winds. The hourly averaged winds were then hand filtered to remove any obviously bad data from the time series, and all winds were linearly interpolated to 250-m height increments above mean sea level up to 15 km. This technique was applied to all data collected by the WPDN profilers during the FIRE Cirrus-II field campaign.

The regional proximity of the WPDN to the FIRE Cirrus-II operational area provides an opportunity for investigation of the wind field throughout the troposphere and lower stratosphere. Apart from the obvious sampling differences between radiosondes and wind profilers, the primary advantage of the WPDN observations is their nominal 1-hour temporal resolution. However, since the length scales resolved by observations spaced at approximately 250 km are on the order of 1500–2000 km (Thiebaux and Pedder 1987; Davies-Jones 1993; Mace 1994), 1-hour temporal resolution may be more than is needed to adequately characterize the synoptic-scale evolution of meteorological features. Therefore, to take full advantage of the temporal resolution of the WPDN data, a time–space conversion scheme is applied. Described in appendix A, this algorithm takes the observations collected 1 hour before and after a particular time and places them along a curved trajectory streamline estimated from the spatial and temporal characteristics of the wind field. The assumption is made that the only acceleration acting on the air parcels is the centripetal acceleration required to maintain the parcels on the curved trajectory. While this scheme effectively coarsens the temporal resolution to 3 hours, the number of observations available every third hour increases substantially, thereby decreasing the uncertainty in horizontal derivatives diagnosed from the wind fields (Davies-Jones 1993). This is especially advantageous in the inner array of the WPDN where, under ideal circumstances, a dense network of observations can be created from the seven available profilers.

The sensitivity of the objectively analyzed quantities to the time–space conversion algorithm was examined. While the qualitative differences between first-order quantities such as divergence and vorticity were not large, quantities derived from the first-order terms such as vertical velocity and ageostrophic wind did show some improvement. For instance, kinematically derived vertical motions (discussed in more detail below) generally have residual vertical velocities at the top of the data column near 14 km where the large-scale ascent is assumed to be negligible. Before the time–space conversion algorithm was applied, these residuals tended to be on the order of 25–50 mb day^{-1}. After application of the time–space conversion algorithm, these residuals decreased to 15–20 mb day^{-1}.

b. Initial processing of radiosonde data

All radiosonde data collected during FIRE Cirrus-II were processed at full vertical resolution. The raw NWS radiosonde data has 6-s (roughly 30 m) vertical resolution and consists of temperature, pressure, humidity, and elevation and azimuth angles. Processing

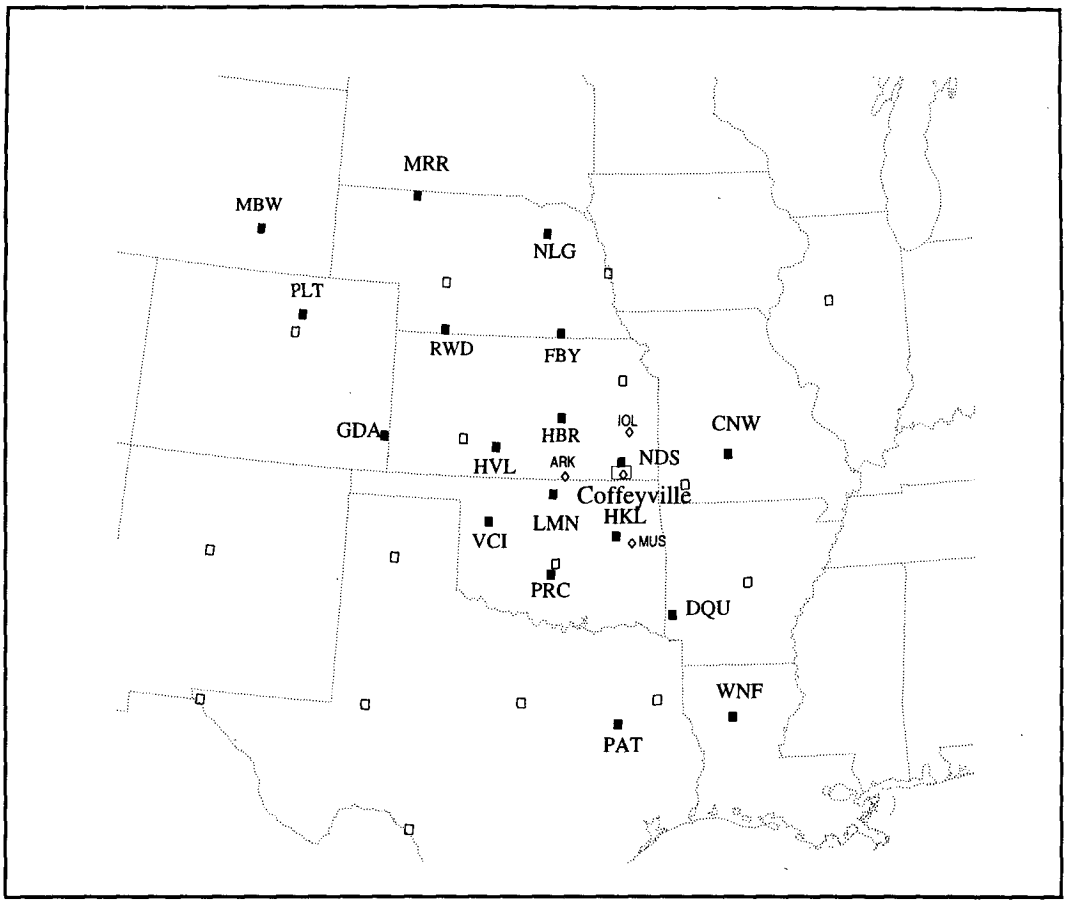

FIG. 1. Map showing the locations of wind profiler and radiosonde sites that were operational during the FIRE II Cirrus Intensive Field Operation during Nov. and early Dec. 1991. The blackened squares represent WPDN sites, the open squares represent operational radiosonde locations, and the open diamonds denote the locations of CLASS radiosonde sites. Coffeyville, Kansas, is denoted by a diamond within an open square.

of the raw data combined several steps designed to generate a research product interpolated to pressure levels at 40–60-m vertical resolution. The data were scanned for obvious or potential errors such as increasing pressure with height or for values that had been previously flagged or interpolated by the NWS processing routines. The raw pressure and elevation and azimuth angle data were smoothed using a variable-width, multipass regression technique designed to reduce root mean square (rms) uncertainty in the derived products. Using the smoothed pressure time series, the time series of standard pressure levels was determined and the observed temperature and relative humidity profiles were interpolated to the standard levels. Location information was generated at the standard pressure levels using the smoothed elevation and azimuth angles. Horizontal winds were then calculated using a centered differencing scheme with the location data. Quality flags were assigned to each sounding using manual inspection.

Further processing of the radiosonde soundings was motivated by the desire to combine the mass and water vapor fields observed by the radiosondes with simultaneous WPDN wind observations. While both sets of observations ultimately complement one another, meshing data from the two observational platform types into a dynamically consistent whole needs to be carefully considered. The wind profilers provide horizontal wind velocities in 250-m layers. The hourly wind reported within a layer closely approximates a true average, being composed of several 6-minute time integrations of the backscattered radar energy from that volume. Radiosondes, however, report nearly instantaneous thermodynamic quantities at approximately 30-m vertical intervals. Since a radiosonde flight takes 1–2 hours and the sensor typically drifts several tens of kilometers during the flight, the vertical profile of a sounding is a collection of individual point measurements, each a function of latitude, longitude, elevation, and time. The four-dimensionality of a sounding is typically not a problem when considering data from the operational radiosonde network. With soundings at 12-h intervals and separated by 400 km, 50-km drift over

a couple of hours does not introduce significant error when considering the temporal and spatial scales that can be resolved by the conventional network. However, during the FIRE Cirrus-II field deployment, radiosonde sites in the Kansas–Oklahoma region were separated by less than half the normal spacing (Fig. 1), and the temporal resolution was enhanced much of the time. Therefore, taking full advantage of the combined radiosonde and wind profiler networks requires a careful accounting of balloon drift and the temporal characteristics of the observations.

The temporal and vertical coordinates defined by the wind profiler observations are specified as the coordinate values to which the radiosonde data are interpolated. This choice is intuitive since enough information exists in each radiosonde sounding to unambiguously interpolate the data to any vertical coordinate; this is clearly not the case for the wind profilers. Additionally, regional kinematic analyses using the wind profiler data are possible at a much finer temporal resolution than from the radiosonde data. For consistency, therefore, physical height will be used as the vertical coordinate in this work.

So that the radiosonde and wind profiler data can be combined into a single diagnostic framework, the vertical resolution of the radiosonde data were coarsened and the soundings were temporally interpolated to approximate the vertical resolution and the nominal times of the wind profiler observations. The soundings were vertically averaged to the same 250-m height increments as the wind profiler data using all available observations 125 m above and below each profiler data level. All data elements in the sounding were treated in this way including the latitudes, longitudes, and times of each observation. After performing the vertical averaging on a time series of soundings from a particular observing site, the layer mean time values were used to temporally interpolate the vertically averaged temperature, pressure, specific humidity, u and v wind components, and latitude and longitude to the top of each hour to match the nominal valid times of the hourly wind profiler data.

This technique, which is similar to one described by Frankhauser (1969), accounts for the drift in the radiosonde during flight and for the time interval of the ascent. Thus, displacements of the sensors in both space and time are considered when performing spatial objective analysis of the data. The most obvious limitation is the temporal resolution of the soundings relative to the wind profiler observations. Therefore, in practice, diagnostics that require thermodynamic information will only be performed at the nominal sounding times. Also, only temporally enhanced sounding periods (3–6 h) are considered when temporal derivatives of the thermodynamic data are necessary. These processing techniques were applied to all radiosonde data collected during FIRE Cirrus-II.

c. *Spatial objective analysis of wind profiler and radiosonde data*

After the initial processing steps have been completed, the wind and thermodynamic data tend to be randomly distributed over the analysis region. In principle, it would be possible to perform spatial objective analysis using the function surface fitting techniques traditionally applied to data of these types: namely, to divide the analysis domain into data polygons, perform function surface fitting of low-order polynomials to the polygon centroids, and conduct a diagnostic analysis directly from the centroid-analyzed data fields (Zamora et al. 1987; Carlson 1989). As shown by Davies-Jones (1993), however, direct examination of the polygon centroid values tends to be most applicable to smaller data networks (from three to seven or so data points) that extend over limited geographical regions. When applied to extended arrays with a variable spatial distribution of data points, it becomes difficult to optimize the function surface fitting technique to reduce the uncertainty in observational and aliasing error at the polygon centroids. Furthermore, interpretation of the centroid results from several polygons is uncertain since polygons of varying spatial extent and geometry have different responses to observational error and to meteorological features below the resolution of the data network (Mace 1994). Therefore, we choose a slightly more involved process that is designed to minimize the influence of observational and aliasing uncertainty.

Initially, the observations are mapped to a 1° latitude–longitude grid using the bivariate interpolation scheme described by Akima (1978, 1984). This algorithm uses the irregularly distributed datapoint positions to divide the analysis domain into triangular cells. Interpolation to the latitude–longitude grid is performed using a fifth-order polynomial surface with coefficients determined from the data triangles. Interpolation from the grid points back to the data points returns the input values to within machine precision. Accuracy away from the data points depends largely on the spatial density of the observations. Not surprisingly, spurious oscillations of the interpolated values are noted when the interpolation grid is much finer than the density of the observations. In order to avoid this undesirable characteristic, the diagnostic domain we consider for quantitative analysis is restricted to the region bounded by the wind profiler locations and enhanced radiosonde sites (Fig. 1). However, all wind profiler and radiosonde sites available are used at each analysis time. In other words, each analysis encompasses most of the western two-thirds of the continental United States. Also, it should be noted here that the radiosonde-observed winds are not used in Kansas or Oklahoma. Inclusion of the radiosonde winds into the wind field analysis in this region caused discontinuities in the time series of kinematic quantities. This inconsistency is likely a reflection of the vastly different

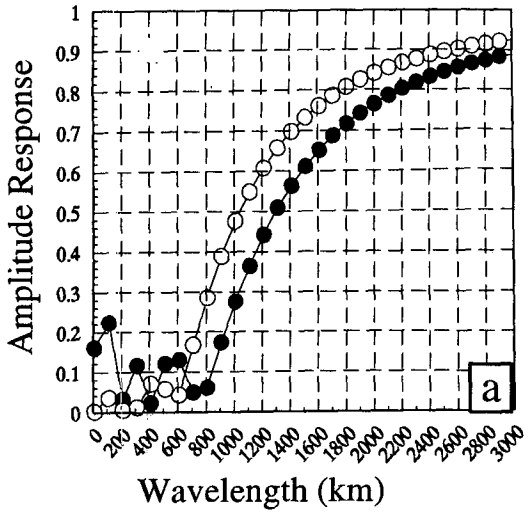

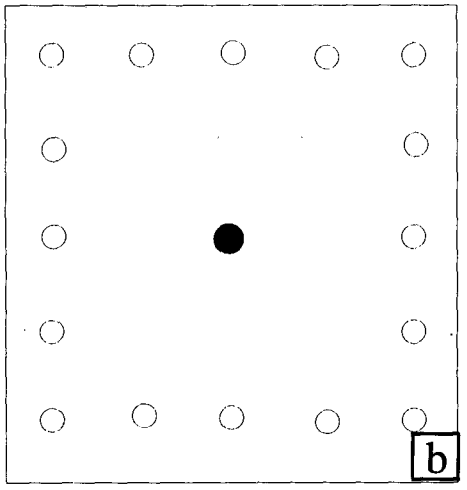

FIG. 2. (a) Amplitude response function of the overdetermined least squares spatial filter described in the text. The solid circles are the amplitude response of the wind speed, and the open circles denote the amplitude response of the vertical component of the relative vorticity. (b) Arrangement of grid points corresponding to the amplitude response curves shown in (a). The solid circle is the central grid point that is being smoothed by the distribution of surrounding gridpoints.

measurement strategies employed by wind profilers and in calculating horizontal winds from radiosondes. Therefore, to maintain consistency in the analysis product, only the profiler winds are considered in the Kansas–Oklahoma region.

The interpolation scheme maps the observed fields exactly without consideration to objective analysis uncertainties. Therefore, the fields mapped to the regular grid are considered to be equivalent to the data in every way. By this it is meant that the observational quantities (u, v, T, p, q) now distributed on the grid contain the desired large-scale atmospheric signal, as well as contributions from random observational error and from atmospheric signal of scale below the network's spatial resolution. Our analysis goal is to filter the data such that only the synoptic-scale atmospheric signal remains. As shown by Thiebaux and Pedder (1987) and Davies-Jones (1993), this analysis goal can be addressed by using overdetermined low-order polynomial surfaces fitted to the geographically distributed data in a least squares sense. Applying these techniques reduces the magnitude of objective analysis uncertainties in a predictable way. In order to remove most small-scale variability from the data, an empirically derived filter based on an overdetermined plane surface is applied to the gridded observations. The distribution of input data and an amplitude response curve of the spatial filter is shown in Fig. 2. The spatial resolution of the smoothed data fields tends to be 2 degrees latitude by 2 degrees longitude, and the rms uncertainty of the analyzed quantities is approximately $\eta 5 \times 10^{-6}$, where η is the uncertainty in the observed quantity. By interpolating the filtered wind fields back to the wind profiler locations, the amount of smoothing can be examined. Shown in Fig. 3, the rms difference between the smoothed and the original data is 3.5 m s^{-1}. While the accepted uncertainty in the wind profiler data is near 2 m s^{-1}, the additional smoothing can be attributed to the filtering of meteorological features below the specified resolution of the analysis grid.

3. Case study: 26 November 1991

The region on which we will concentrate for quantitative analysis is bounded by southern Nebraska, eastern Colorado, northern Texas, and western Missouri and Arkansas. This area, which encloses the densest

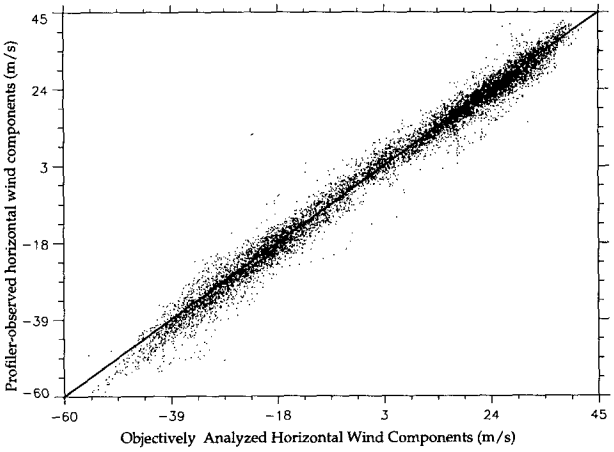

FIG. 3. Scatter diagram of the objectively analyzed horizontal wind components (abscissa) compared with the wind profiler-observed horizontal wind components (ordinate). The units are m s^{-1}. The rms difference in the objectively analyzed components and the observations is 3.2 m s^{-1}.

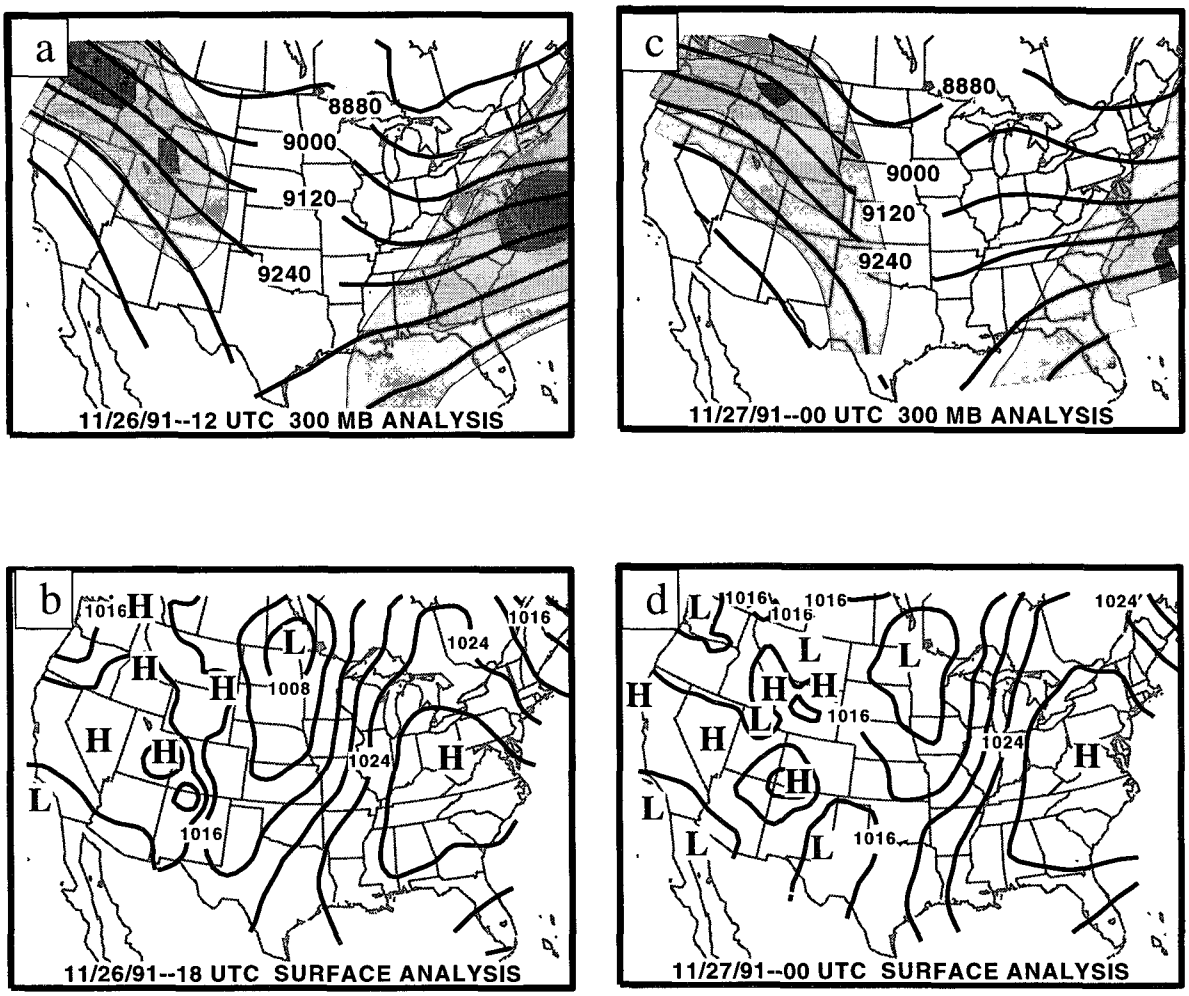

FIG. 4. The synoptic setting for the case study period under consideration. (a) 300-mb heights and isotachs at 1200 UTC 26 Nov. 1991. (b) Surface pressure analysis at 1800 UTC 26 Nov. 1991. The contour interval is 4 mb for the surface pressure and 60 m for the thickness. (c) 300-mb heights and wind vectors at 0000 UTC 27 Nov. 1991. Plotting convection as in (a). (d) Surface pressure at 0000 UTC 27 Nov. 1991. Plotting convention as in (b).

network of wind profiler and radiosonde sites (Fig. 1), will be referred to as the analysis domain. Within this domain, the wind observations are supplied exclusively by the WPDN. Outside of this region, the radiosonde-derived winds are used in the objective analysis scheme but are not displayed here or considered for quantitative application. We examine the period from 1800 UTC 26 November 1991 (26/18) to 0000 UTC 27 November 1991 (27/00).[1] This period is chosen for several reasons. All radiosonde sites in the western two-thirds of the United States began a 3-hour launch schedule at 26/12. This enhanced sounding period coincided with two distinct synoptic-scale upper-tropospheric cloud systems west of the Mississippi, one of which propagated through the analysis domain and was sampled by surface-based instrumentation and research aircraft at Coffeyville.

a. Synoptic setting

The synoptic setting for this period is shown in Fig. 4. A small amplitude ridge–trough pattern was established over North America early on 26 November. Northwesterly flow in the upper troposphere ahead of the offshore ridge existed over the West Coast, while a broad diffluent trough is analyzed in the central United States. A strong jet is embedded in the northwesterly flow over the western third of the United States. Speed maxima of more than 60 m s^{-1} were observed by radiosondes in southwestern Wyoming and the Pacific Northwest. In the Kansas–Oklahoma region wind speeds decreased substantially compared to the

[1] Date–time indicated as day (November)/two digit hours (UTC).

West, and the flow became diffluent in the upper troposphere. At the surface the western United States was dominated by a region of high pressure under the broad upper-level ridge, while low pressure and an associated frontal system were situated in the central United States. The analysis area was influenced by a broad southerly flow east of the surface trough. The southerly flow extended from the Gulf of Mexico into southern Canada.

By 27/00, a general amplification of the long-wave pattern is noted. Heights were rising over the Rocky Mountain states at 300 mb (Fig. 4c), while height falls occurred over the Pacific coast and central United States. A small amplitude trough is evident at 300 mb extending from the western Gulf of Mexico into southern Canada. The northwesterly jet had become firmly established in the region of rising heights over the Rocky Mountain states. The exit region of the jet had propagated into the analysis domain, and a strong wind speed gradient existed from east Texas northward to the Dakotas. At the surface (Fig. 4d) the low in the north-central United States and the associated frontal system had propagated eastward and filled slightly.

Figure 5 shows Geostationary Operational Environmental Satellite (GOES) infrared (IR) imagery for this period. While cold cloud tops denoting optically thick cirrus cover much of the western one-half of the United States, two identifiable broad-scale features can be identified. The easternmost of these is oriented perpendicular to the upper-tropospheric flow and extends through central Oklahoma and into central and eastern Kansas. The east–west scale of this system increases considerably in the northern Plains and extends from central Nebraska to the western Great Lakes. This system bears a resemblance (at least in its southern portions) to a baroclinic leaf cirrus system (Weldon 1979; Starr and Wylie 1990). This system appears to be correlated with the deepening surface low and amplifying upper-tropospheric disturbance identified above. Cirrus westward of the Rocky Mountains, on the other hand, is associated with the amplifying upper-tropospheric ridge. Cloud patterns here suggest an alongstream orientation with optically thick cirrus occurring near the ridge axis and progressively thinner and more patchy clouds extending to the flow inflection downstream of the ridge axis. This large-scale cloud pattern is readily classified as a ridge-crest cirrus system in accordance with Starr and Wylie (1990).

b. Kinematic analysis

The 10-km profiler-derived wind field in the analysis region at 26/18 and 27/00 is shown in Fig. 6. This height corresponds to the level of maximum wind speed in the northwesterly jet. The strong speed gradient associated with the exit region of the northwesterly jet is quite evident. A well-defined minimum in horizontal wind speeds can be seen in association with the trough axis that extended through central Oklahoma and Kansas at this time. By 27/00, the main features in the wind field at 10 km had propagated eastward at approximately 12 m s^{-1} (Fig. 6b). The region of sharpest cyclonic turning in the wind field is now analyzed in extreme western Missouri and Arkansas. The jet axis is identifiable at 27/00 extending through Colorado into the panhandle region of Oklahoma, and the intense isotach gradient between the jet core and trough axis is squarely within the wind profiler network. It is evident that air exiting the jet core in western Oklahoma experienced rapid deceleration as it flowed southeastward toward the trough axis.

The horizontal divergence and relative vorticity at 10 km are shown in Fig. 7. At 26/18, a maximum in positive vorticity is located over the panhandle of Oklahoma with positive values extending eastward to western Missouri and Arkansas. The trough axis that was situated in eastern Oklahoma at 26/18 (Fig. 6b) is not clearly delineated in the vorticity field. The observed vorticity over Oklahoma and Kansas will be shown to be due to horizontal speed shear associated with the jet and cyclonic turning in the low amplitude trough. By 27/00, however, the north–south oriented axis of positive vorticity (Fig. 7d) is more clearly aligned with the trough axis identifiable in the wind field (Fig. 6b). Values near the trough axis have increased during the previous 6 hours. This is indicative of an overall amplification of the upper-tropospheric wave pattern.

The horizontal divergence at 10 km is also closely coupled to the advancing jet streak and to the shortwave trough. At 26/18, an axis of positive horizontal divergence was oriented through central Oklahoma west of the trough axis and east of the maximum wind speed gradient (Fig. 7a). Convergence was diagnosed in the speed gradient from the panhandle region northward. At 27/00 (Fig. 7c), the southern portion of the divergence axis at 10 km had shifted eastward with the propagating and evolving wind field, while the more northerly portions had remained stationary. This is consistent with the jet core advancing into Oklahoma and the trough axis moving eastward. Also, the maximum in horizontal divergence along this axis had shifted northward at 27/00, although the central Oklahoma maximum at 26/18 had moved beyond the coverage of the WPDN. An axis of horizontal convergence becomes identifiable at 27/00 aligned along the northwesterly jet core (Fig. 6b) through Colorado and into the Oklahoma panhandle. A maximum in horizontal convergence occurs in the jet core over the Red River.

Since the horizontal divergence is closely coupled to the ageostrophic motions and vertical velocity and is therefore important to cirrus cloud formation on large scales, it is instructive to examine in greater detail the individual components of this quantity. Using a natural coordinate system oriented with the wind flow, the horizontal divergence can be written

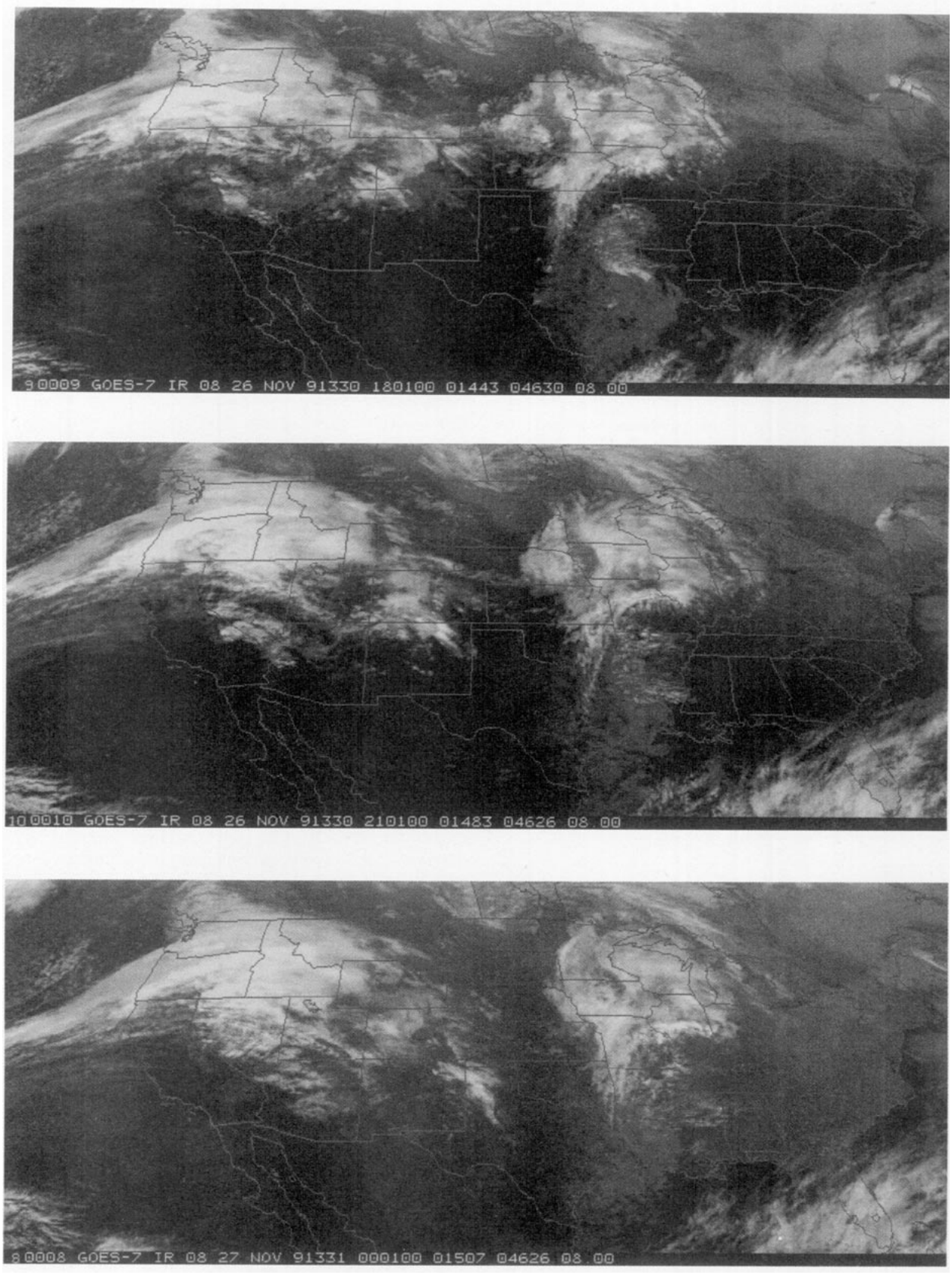

FIG. 5. Infrared satellite imagery: (a) 1800 UTC 26 Nov., (b) 2100 UTC 26 Nov., (c) 0000 UTC 27 Nov. 1991.

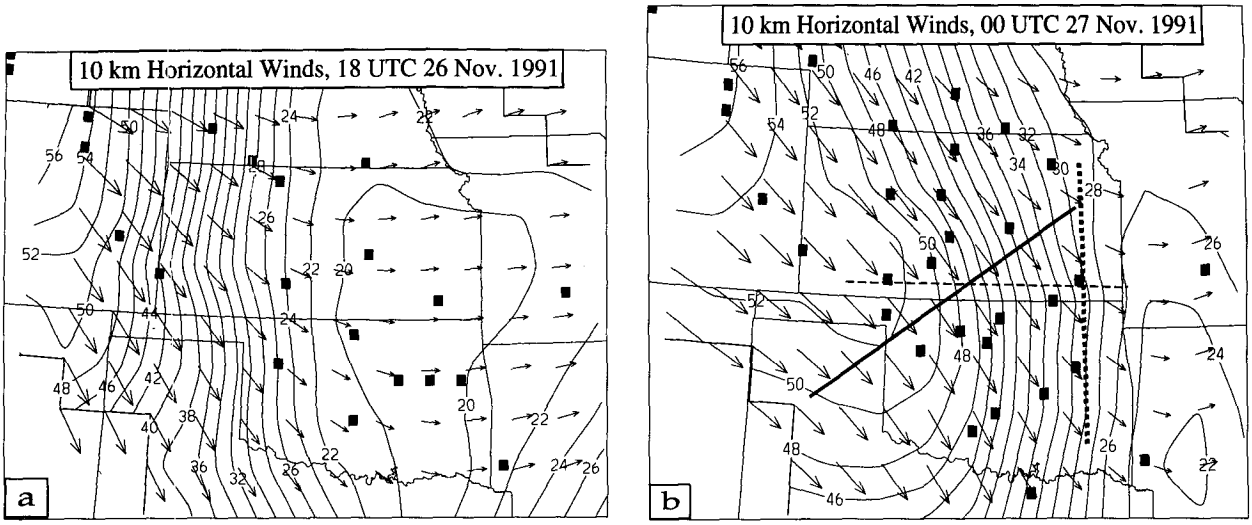

FIG. 6. Horizontal wind vectors and speeds analyzed from the time–space converted WPDN data at (a) 1800 UTC 26 Nov. 1991 and (b) 0000 UTC 27 Nov. 1991. The wind vectors are compass direction, and the vector lengths are proportional to wind speed. The contours are of wind speed in m s^{-1}. The contour interval is 2 m s^{-1}. The solid squares denote the location of wind profiler observations used in the objective analysis. The straight solid, dashed, and dotted lines in (b) denote the location of horizontal cross sections discussed later in the text.

$$\text{div} = \frac{\partial U}{\partial s} - U\frac{\partial \beta}{\partial n} + \frac{U}{R_t}, \qquad (1)$$

where U is the horizontal wind speed, s is directed along the observed airflow, n is directed to the right of the motion, β is the wind direction, and R_t is the radius of trajectory curvature. The first term on the right of Eq. (1) accounts for the divergence of air parcels along the direction of motion, the second term quantifies the difluence of streamlines, and the third term is due to advection of trajectory curvature by the mean wind. Following Cammas and Ramond (1989), the along- and cross-stream gradients are calculated where

$$\frac{\partial}{\partial s} = \mathbf{s}\cdot\nabla = \frac{1}{U}\mathbf{V}\cdot\nabla = \frac{1}{U}\left(u\frac{\partial}{\partial x} + v\frac{\partial}{\partial y}\right)$$

$$\frac{\partial}{\partial n} = \mathbf{n}\cdot\nabla = \frac{1}{U}\nabla\cdot(\mathbf{k}\times\mathbf{V}) = \frac{1}{U}\left(-v\frac{\partial}{\partial x} + u\frac{\partial}{\partial y}\right).$$

The curvature advection term in Eq. (1) is determined as a residual by differencing the Cartesian coordinate representation of the horizontal divergence and the sum of the speed divergence and directional difluence terms. For the case considered here the contribution to the horizontal divergence by the curvature advection remained at least a factor of 5 smaller than the sum of the first two terms on the right of Eq. (1).

The contribution of the natural coordinate components of the horizontal divergence at 10 km is shown in Fig. 8. A large degree of cancellation can be seen between the speed and directional difluence terms. The directional difluence, however, did tend to be slightly more positive (Fig. 8b) than the speed difluence was negative (Fig. 8a) in central and eastern Oklahoma at 26/18. Not unexpectedly, the speed difluence was negative or convergent in the exit region of the strong jet, while directional difluence was positive ahead of the speed gradient. The cancellation vanished, however, ahead of the speed gradient in eastern Oklahoma at 26/18 where the speed difluence was weakly positive, while the directional difluence in the trough resulted in positive values of the total horizontal divergence. The contribution due to curvature advection was positive in the region of cyclonic turning (Fig. 8c), although the magnitudes tended to be much smaller. Interestingly, the axis of the divergent contribution due to curvature advection is displaced west of the trough axis. This displacement is due to the lower relative wind speeds in the trough axis. While the maximum cyclonic curvature was in eastern Oklahoma (roughly parallel to the 1×10^{-6} s^{-1} isopleth in Fig. 8c), the wind speeds and curvature correlated most positively approximately 200 km west of the trough axis.

The changes in the natural coordinate contributions to the horizontal divergence between 26/18 and 27/00 are consistent with the eastward propagation of the wind field. Since the exit region of the jet is more squarely within the profiler array at 27/00, the resolution of the divergence components is more certain. Directional diffluence tends to remain dominant in eastern Oklahoma, while a region of directional confluence is resolved extending from western Oklahoma into northeastern Colorado. The axis of speed confluence now extends northward from south-central Oklahoma and curves northeastward along the wind speed gradient

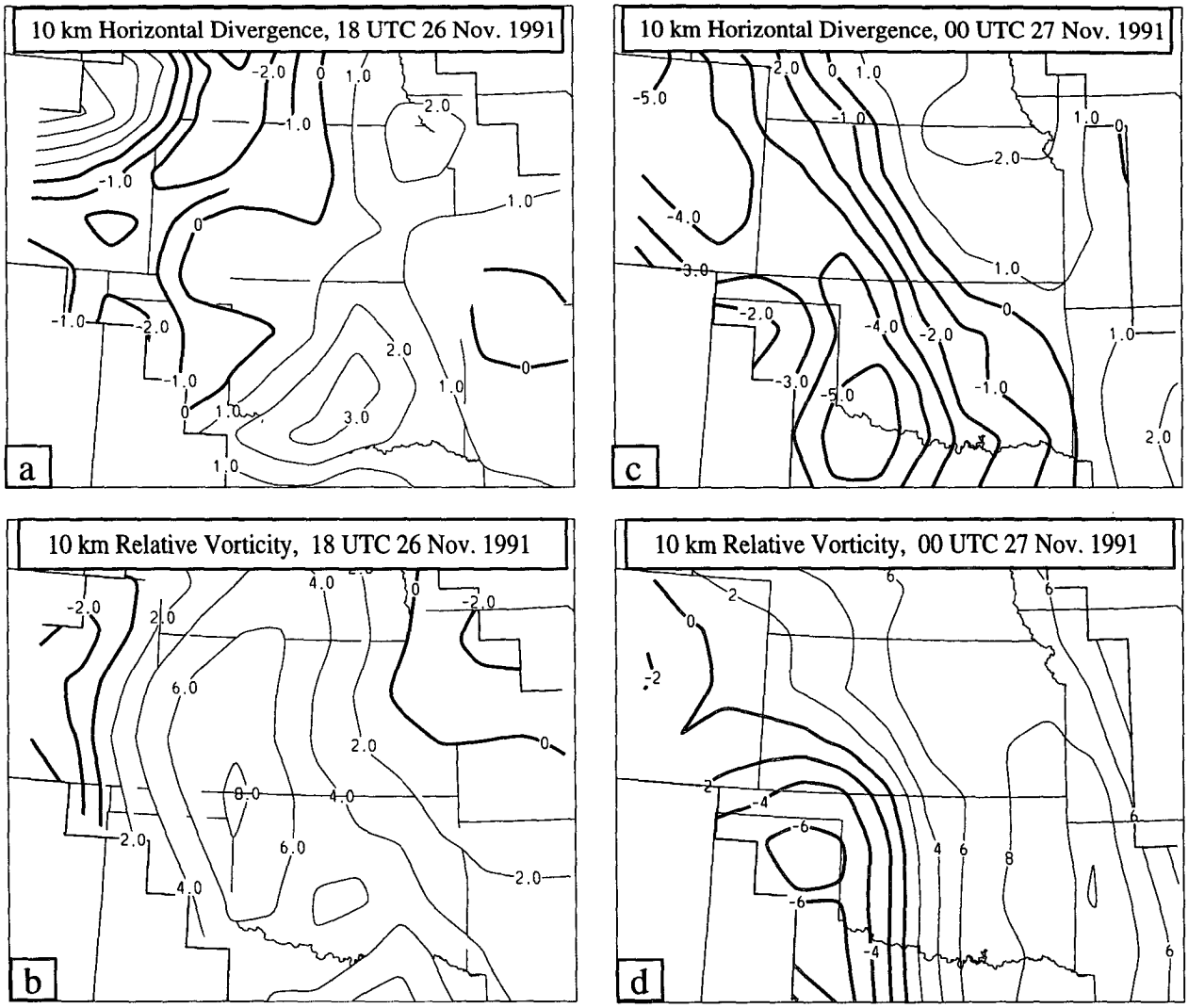

FIG. 7. 10-km horizontal divergence and relative vorticity: (a) 1800 UTC 26 Nov. horizontal divergence, (b) 1800 UTC 26 Nov. relative vorticity, (c) 0000 UTC 27 Nov. horizontal divergence, and (d) 0000 UTC 27 Nov. relative vorticity. The contour interval in (a) and (c) is 1×10^{-5} s^{-1} and in (b) and (d) 4×10^{-5} s^{-1}. Thick solid lines denote negative contours.

west of the trough axis. While the trough remains evident in southwestern Missouri and northwestern Arkansas in the curvature term, the primary contribution over the analysis region is convergent owing to anticyclonic curvature in the wind speed gradient.

The ageostrophic winds were estimated using the horizontal momentum equations after Zamora et al. (1987):

$$\frac{dv}{dt} = \left(\frac{\partial}{\partial t} + u\frac{\partial}{\partial x} + v\frac{\partial}{\partial y} + w\frac{\partial}{\partial z}\right)v = -fu_a$$

$$\frac{du}{dt} = \left(\frac{\partial}{\partial t} + u\frac{\partial}{\partial x} + v\frac{\partial}{\partial y} + w\frac{\partial}{\partial z}\right)u = fv_a,$$

where u_a and v_a are the eastward and northward components of the ageostrophic wind, respectively, and w is the vertical motion calculated using the kinematic method described in appendix B. Time derivatives were estimated using centered differencing. Uncertainties in the kinematic vertical velocity are discussed in appendix B; however, we assume an overall uncertainty of 2 cm s^{-1} in this term. The ageostrophic components will be most influenced by this uncertainty in regions of strong vertical shear where the horizontal gradient of u and v are small (e.g., below the level of maximum wind along the jet axis). If we assume a vertical shear of 10 m s^{-1}/km in a horizontal wind component and an uncertainty of 2 cm s^{-1} in the vertical velocity, this translates to an uncertainty in the ageostrophic wind speed of about 2 m s^{-1}.

To further delineate between the components of the ageostrophic wind in the along- and cross-stream di-

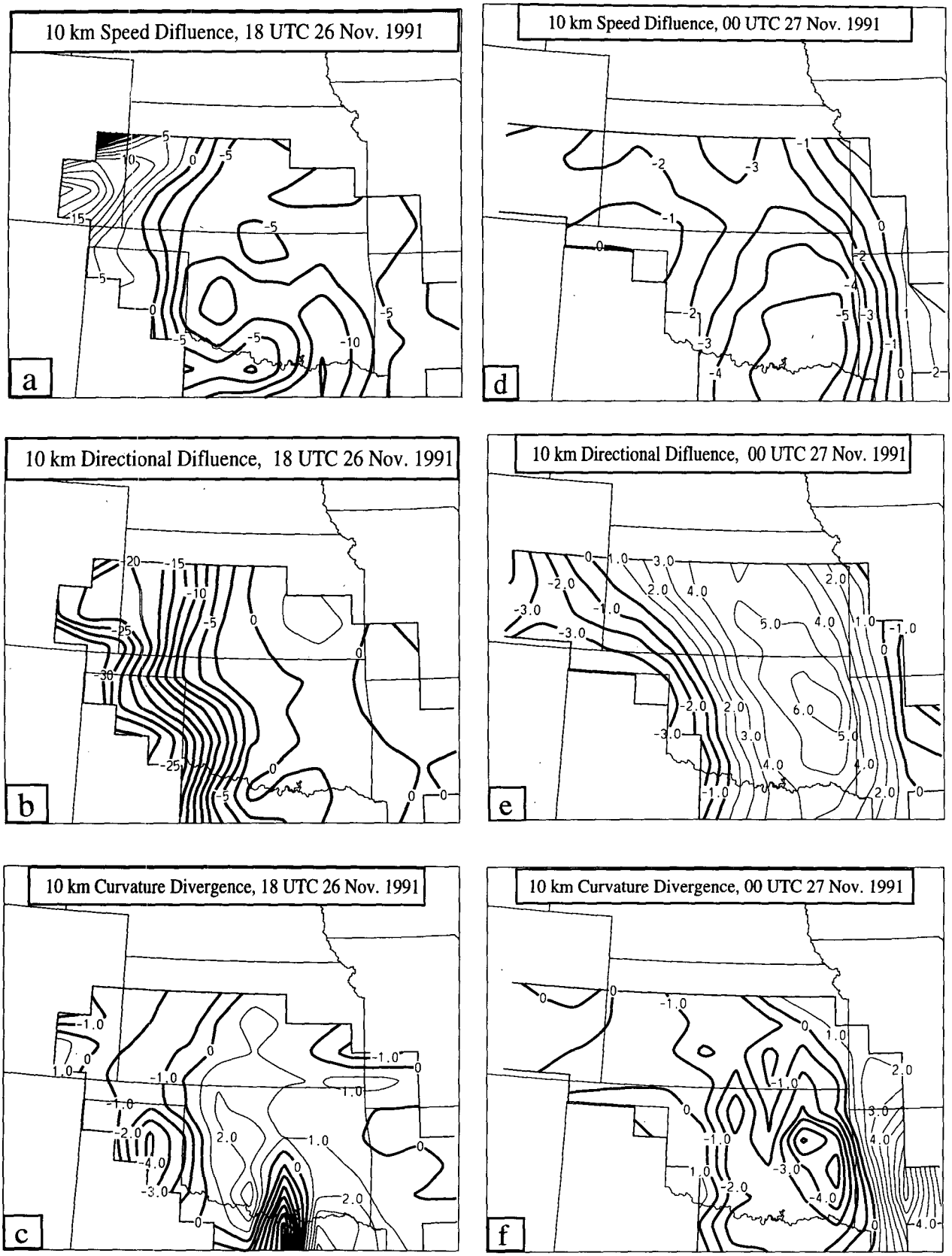

FIG. 8. Natural coordinate components of the horizontal divergence: (a) 1800 UTC 26 Nov. speed difluence, (b) 1800 UTC 26 Nov. directional difluence, (c) 1800 UTC 26 Nov. curvature advection, (d) 0000 UTC 27 Nov. speed difluence, (e) 0000 UTC 27 Nov. directional difluence, and (f) 0000 UTC 27 Nov. curvature advection. Plotting convention as in Fig. 7 except contour interval for the curvature advection is 1×10^{-5} s^{-1}.

rections, consider the natural coordinate components of the ageostrophic wind in a frictionless atmosphere (Cammas and Ramond 1989):

$$V_{an} = +\frac{1}{f}\frac{dU}{dt}$$

$$V_{as} = -\frac{1}{f}\frac{U^2}{R_t},$$

where V_{an} and V_{as} are the cross- and alongstream components of the ageostrophic wind, respectively. It can be seen that the cross-stream ageostrophic wind is due primarily to alongstream accelerations of air parcels while ageostrophic motions along the airstream arise from centripetal accelerations on curved trajectories.

The ageostrophic winds and their associated natural coordinate components at 10 km are shown in Fig. 9. The influence of the trough and the jet exit region are the dominant factors at this level. While V_{an} nearly vanishes near the trough axis in eastern Oklahoma and Kansas, the influence of the jet exit region is evident (to a greater extent at 27/00) with ageostrophic flow to the right of the wind indicative of the deceleration of air parcels as they pass from the jet core into regions of weaker pressure gradient. This pattern of V_{an} also suggests a transverse ageostrophic circulation that is thermally indirect in the jet exit. This will be considered in more detail below. While the transverse ageostrophic flow is negligible near the trough axis, the observed winds are subgeostrophic here, as expected, at 26/18 and 27/00. This can be seen by examining the V_{as} field. At 26/18, the trough axis (Fig. 6a) is not clearly identifiable in the V_{as} field, although the region of negative V_{as} in Oklahoma and Kansas correlates well with the rather broad region of cyclonic turning seen in the wind field. By 27/00, subgeostrophic flow is concentrated along the trough axis delineated by the region of negative V_{as} in eastern Oklahoma and Kansas and western Missouri and Arkansas. The alignment of the subgeostrophic flow regime along the trough axis and the apparent increase in magnitude of negative V_{as} support the hypothesis that the flow was amplifying during this period. Also at 27/00, large positive values of V_{as} are resolved over much of the western portion of the analysis region. Positive values of V_{as} indicate that air parcels in this region are following anticyclonic trajectories. This hypothesis can be examined by considering the curvature contribution to the relative vorticity at 27/00. Shown in Fig. 10, these values were calculated as a residual by differencing the shear vorticity and total Cartesian representation of the relative vorticity. The streamline curvature in the western portions of the analysis region was clearly negative. When anticyclonic streamlines move eastward at phase speeds slower than the wind speed, the resulting radii of trajectory curvature tend to be less negative than the streamline curvature since parcels are moving through the advancing streamline pattern (Holton 1979). While the eastward progression of the anticyclonically curved exit region would have resulted in less negative values of the trajectory curvature, the relatively slow phase speed of the pattern relative to the airflow would still lead to a negative trajectory curvature and positive alongstream ageostrophic flow in this region.

The diagnostic framework provided by the natural coordinate representation of the ageostrophic winds aids in an understanding of the pattern of upper-tropospheric divergence shown in Fig. 7. Consider the ageostrophic wind vectors and speeds at 27/00 (Fig. 9d). An axis of horizontal convergence is suggested extending from south-central Kansas to north-central Texas. This feature is also evident at 26/21 (not shown) where it extended in a north–south direction from western Kansas through the Texas panhandle. Since the geostrophic winds are nondivergent (neglecting meridional advection of the earth's vorticity), the horizontal divergence is closely coupled to the ageostrophic wind. It is not surprising then to find a close correspondence between the convergence resolved from the total wind field and the axis of convergence in the ageostrophic winds in this region. The convergence in western Oklahoma was induced by a superposition of the ageostrophic flow near the trough east of the convergence axis, the transverse ageostrophic flow associated with the jet exit and the ageostrophic wind induced by the anticyclonic parcel trajectories in the western portion of the analysis region.

The transverse ageostrophic flow and horizontal divergence pattern at 10 km suggest a thermally indirect circulation across the jet exit region. A vertical cross section of the horizontal wind at 26/21 through the analysis domain and normal to the upper-tropospheric flow is shown in Fig. 11a. The jet streak is evident in the southern half of the cross section with a strong vertical shear between 7 and 10 km. The cross-stream ageostrophic winds (Fig. 11b), as expected, reach maximum magnitudes in excess of 30 m s^{-1} in the jet portion of the cross section and become positive (to the left of the flow) in the middle and lower troposphere. The vertical motions in the plane of the cross section (Fig. 11c) show ascent, maximizing in the middle troposphere at just over 3 cm s^{-1}, across the northern half of the cross section under the upper divergence discussed above. Descent is diagnosed farther south under the elevated convergence region. By simply combining the vertical motion and the transverse ageostrophic wind into vertical and horizontal vector components, a qualitative image of the transverse ageostrophic circulation can be plotted (Fig. 11d). Overlaying the derived vector field on the potential temperature pattern in the cross section, we find ascent in the relatively colder air north of the jet axis while the warmer air beneath the jet core is descending. In other words, we diagnose a thermally indirect transverse circulation centered near 5 km. The horizontal gradient of the vertical motion is clearly frontogenetical here with vertical gradients in

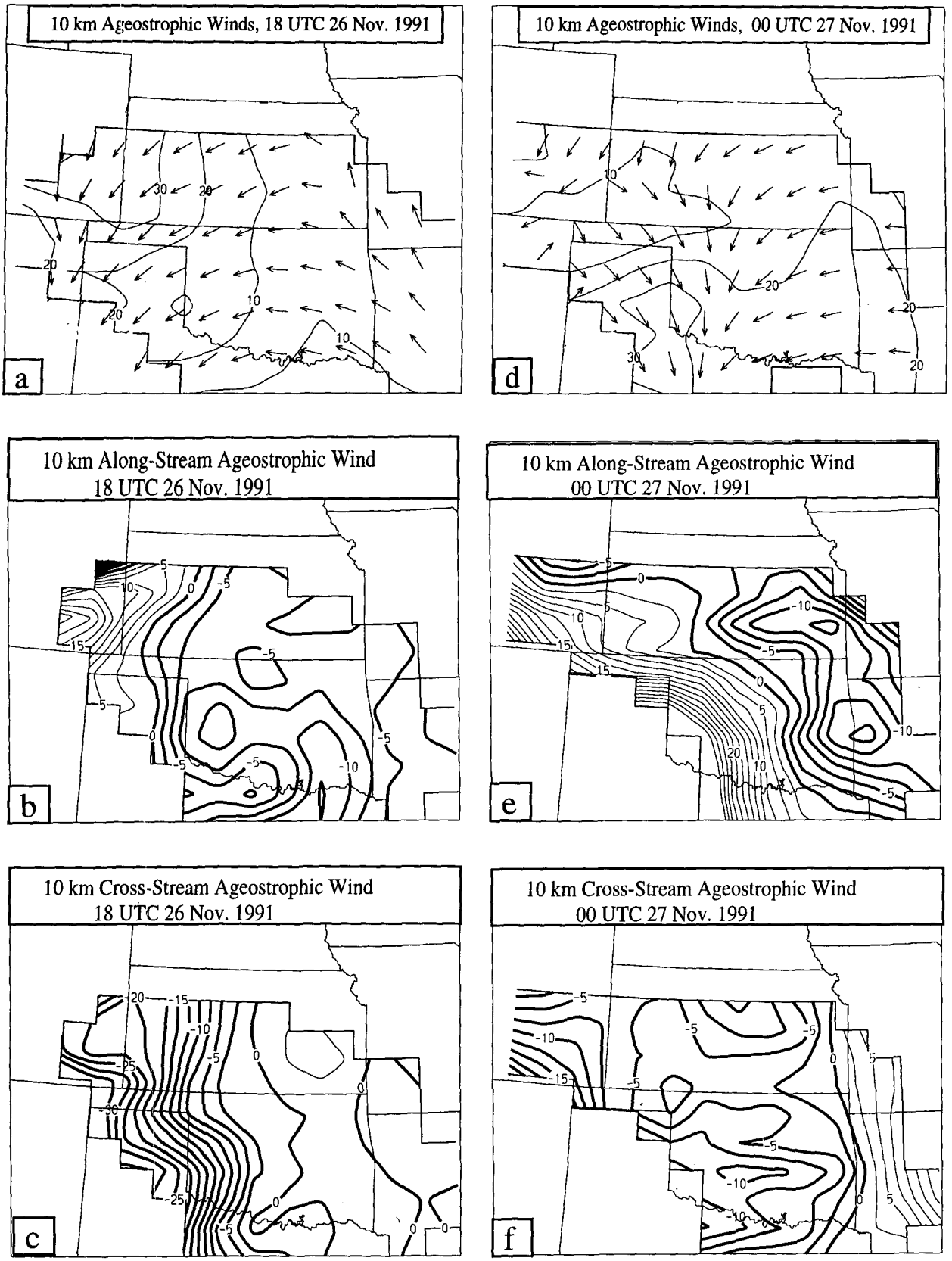

FIG. 9. Ageostrophic wind and natural coordinate components of the ageostrophic wind: (a) 1800 UTC 26 Nov. ageostrophic vectors and speeds, (b) 1800 UTC 26 Nov. alongstream component, (c) 1800 UTC 26 Nov. cross-stream component, (d) 0000 UTC 27 Nov. ageostrophic vectors and speeds, (e) 0000 UTC 27 Nov. alongstream component, and (f) 0000 UTC 27 Nov. cross-stream component. The vectors in (a) and (d) as in Fig. 6 with a contour interval of 10 m s^{-1}. The contour interval in (b), (c), (e), and (f) are 5 m s^{-1} with negative values contoured with thicker lines.

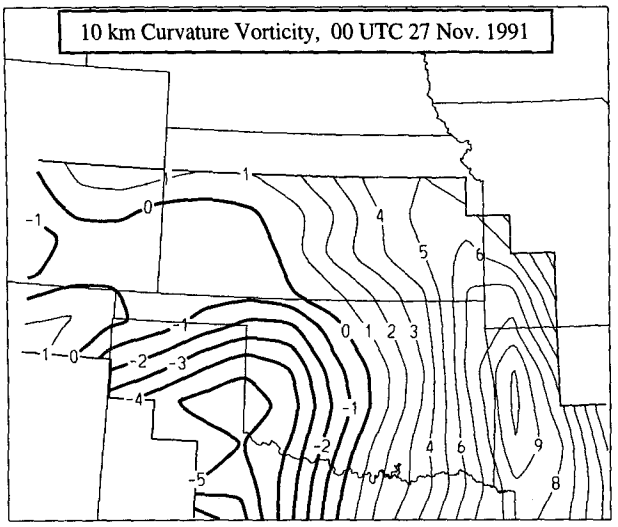

FIG. 10. Curvature component of the relative vorticity at 0000 UTC 27 Nov. The contour interval is 1×10^{-5} s^{-1} with negative values contoured with bolder lines.

potential temperature being tilted into the horizontal plane.

An interesting characteristic of the transverse ageostrophic circulation diagnosed late on 26 November is the placement of the circulation to the cyclonic side of the jet axis. While a thermally indirect transverse circulation is expected in the exit region of a jet streak (Keyser and Shapiro 1986), the circulation cell would tend to be centered on the jet axis in the absence of thermal advection. The orientation diagnosed here places subsident vertical motions beneath the advancing jet core. Unfortunately, the anticyclonic shear side of the jet was not sampled by the profiler array during this time. We are, therefore, unable to determine what the characteristics of the vertical motions were to the right of the jet axis. However, by building on the previous discussion of the kinematic characteristics of the upper troposphere, understanding the orientation of the ageostrophic circulation in the left exit region is straightforward. The displacement of the indirect circulation resulted from the juxtaposition of the diffluent trough axis in the northeast of the analysis domain, the jet exit region, and the anticyclonic curvature in the west. The upper-tropospheric divergence in the region of directional diffluence and small but positive curvature divergence coupled with lower-tropospheric convergence associated with the weak front and developing low pressure forced the ascending branch of the circulation. While the influence of streamline curvature on the horizontal divergence was small in the northeast areas, the westerly ageostrophic motions that resulted from the positive curvature (Fig. 9) contributed to the development of upper-tropospheric convergence west of the trough axis (Fig. 7). This convergence was strengthened by a confluence of the northeasterly ageostrophic flow in the jet exit region (caused by alongstream parcel decelerations, Fig. 9) and the positive alongstream ageostrophic flow associated with anticyclonic trajectories (Fig. 10) beneath the jet core. This resulted in strong upper-tropospheric convergence over western Oklahoma and Kansas forcing the diagnosed descent in this region.

Transverse ageostrophic circulations associated with jet flows can also be interpreted in terms of the Sawyer–Eliassen equation (Keyser and Shapiro 1986). This equation diagnoses a streamfunction that arises under the constraint that thermal wind balance be maintained and is forced by a combination of geostrophic stretching and shearing deformations acting on thermal gradients. We found that the forcing of the Sawyer–Eliassen equation is negative (as required for a thermally indirect circulation) and reaches maximum magnitudes to the left of the jet core approximately 3 km above the diagnosed center of the transverse circulation shown in Fig. 11d. The primary contribution to the forcing arises from a weakening of the near-jet thermal gradients by the geostrophic stretching deformation. The ageostrophic vertical circulation that was diagnosed from the wind profiler data then acts to maintain thermal wind balance by strengthening the frontal contrast being weakened by the geostrophic wind.

c. The cloud event of 26 November: Regional and local description

The analysis of the objectively analyzed radiosonde and wind profiler data has enabled us to infer the dynamical characteristics of the large-scale flow during the period under consideration. However, our primary goal is to understand how the cloud fields (cirrus, in particular) evolved in concert with the dynamics. Indeed, it is this connection between the large-scale dynamical characteristics and the macroscopic properties of the resulting clouds that will ultimately be combined with the observed microphysical and radiative properties to yield improved parameterizations of cloud occurrence and optical properties in GCMs.

Consider again the GOES satellite imagery (Fig. 5) of the cloud band as it progressed over central and eastern Kansas and Oklahoma from 26/18–27/00. At 26/18, the cloud system appeared as a linear feature oriented approximately south–north from central Texas through Oklahoma and into eastern Kansas where the system broadened into a fairly extensive cloud system centered over Iowa. In north Texas the band appears to be composed primarily of middle-level clouds, while the clouds become progressively brighter and more cirriform in nature from central Oklahoma northward. The horizontal width of the band increases from approximately 100 km in central Oklahoma to more than 250 km in northeast Kansas. It is important to note here that this particular cirrus system cannot be classified as a typical jet stream cirrus event where cirrus is often ob-

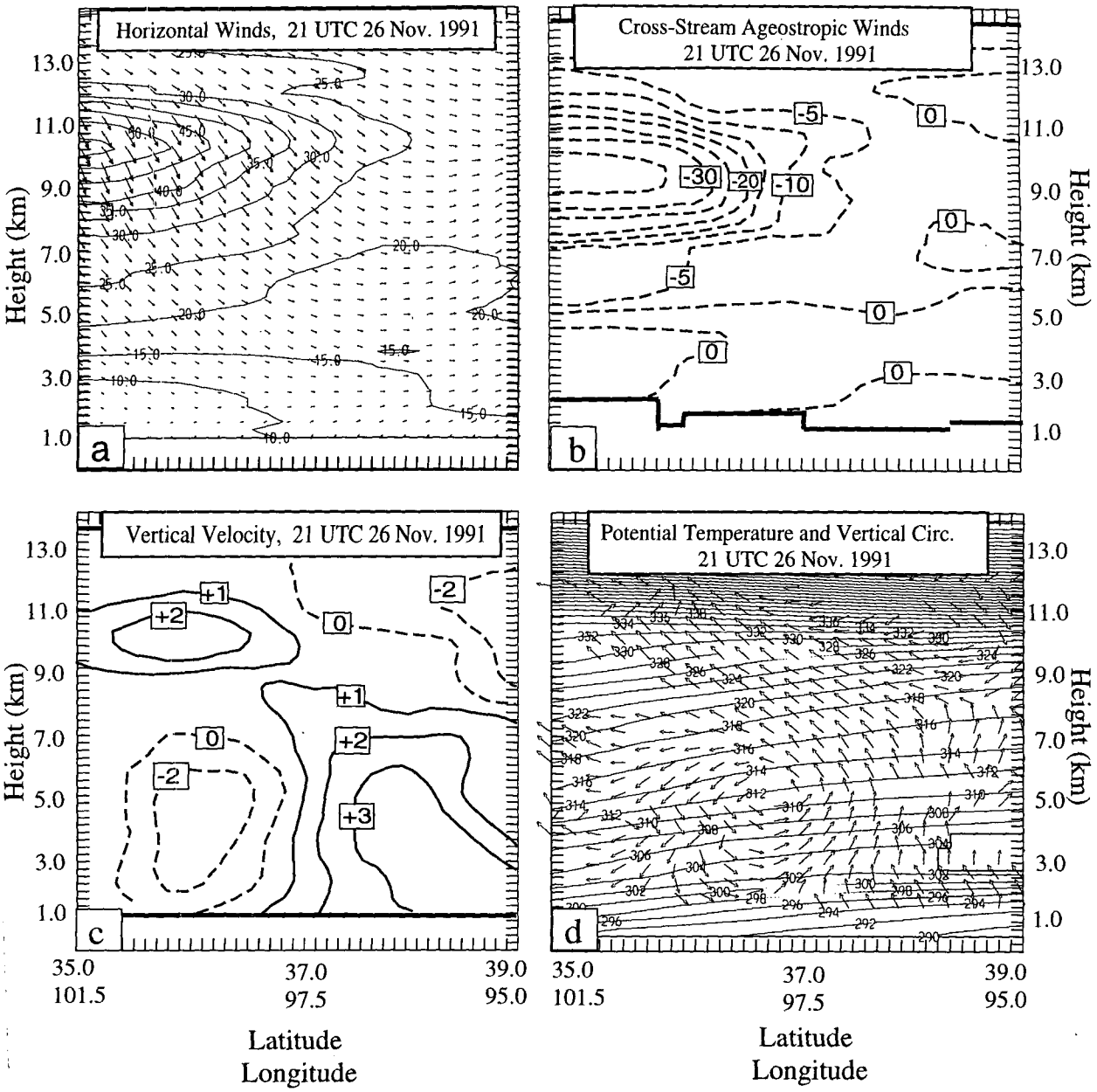

FIG. 11. Horizontal cross section at 2100 UTC 26 Nov. along the thick straight line shown in Fig. 6. The cross section is oriented such that the left side of the plot is the southern end of the solid line in Fig. 6b. (a) Horizontal wind vectors and speeds. The vectors are compass direction with north toward the top of the page, and the contour interval is 5 m s^{-1}. (b) The cross-stream component of the ageostrophic wind. Contour interval is 5 m s^{-1}. (c) The kinematically derived vertical velocity. The contour interval is 2 cm s^{-1}. (d) The ageostrophic circulation vectors are derived by combining the fields in (b) and (c). The vectors are overlain on the potential temperature contoured at a 2-K interval.

served to be elongated parallel to the wind flow. The upper-tropospheric flow here is generally perpendicular to the orientation of the broad-scale cloud field, and the system propagates roughly at the phase speed of the dynamical pattern. East of the cloud band in Texas, Oklahoma, and Arkansas, low and middle-level clouds with some cirrus were associated with a developing southerly flow from the Gulf of Mexico. Skies cleared considerably in western Kansas and the panhandle region of Oklahoma and Texas.

The high cloud optical depths calculated using visible *GOES-7* data and the technique of Minnis et al. (1993) are shown in Fig. 12. Optically thin cirrus is diagnosed along much of the band through central Oklahoma. Optical depths increase substantially in southern Kansas. It is noteworthy that a simple exam-

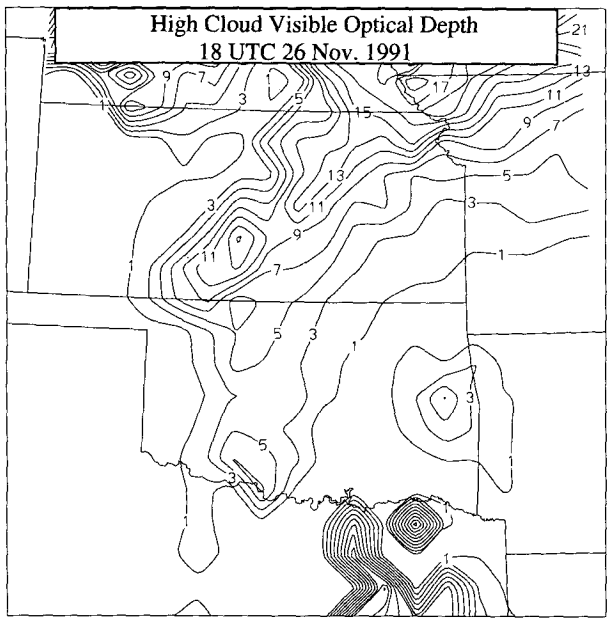

FIG. 12. High cloud visible optical depths derived from GOES data at 1800 UTC 26 Nov.

ination of the IR imagery does not suggest a large change in the character of the cloud band in south-central Kansas. While some variability in the brightness is evident, no large changes occur in the IR from central Oklahoma into northern Kansas. However, at visible wavelengths the southwest–northeast oriented spur of cirrus in south-central Kansas identifiable in the infrared imagery represents the southern extent of the optically thickest cloud line. We speculate that these characteristics are evidence of the well-known property of thin cirrus that the infrared emissivity approaches unity more rapidly than the visible reflectivity (Ackerman et al. 1988).

By 26/21, the entire cloud structure had progressed eastward. The leading edge of the main cloud band in the infrared imagery is identified in eastern Texas and Oklahoma. Evaluation of the satellite-derived visible optical depths are not possible at 26/21 due to increasing solar zenith angles. Farther north in northeastern Oklahoma and southeast Kansas, a series of three southwest–northeast oriented cloud lines are identified. Animation of the imagery suggests that these lines were becoming increasingly brighter with time, indicating active cirrus generation, and propagating southeastward toward the leading edge of the primary cloud system. Apparently, cloud generation was occurring in a wavelike pattern oriented nearly parallel to the weak southwesterly flow aloft. The southwestern portion of these active generation regions tended to be advected faster toward the east by the advancing jet streak (Fig. 6) than the northeastern segments. This resulted in the north–south orientation of the cloud line in the infrared imagery. This is particularly evident between 26/21 and 27/00. Figure 13 shows the brightest band as it passed through southeast Kansas between 26/21 and 27/00. The initial southwest–northeast orientation at 26/21 gradually became more north–south as the southern portions were more rapidly advected eastward relative to the northern parts.

By 27/00, the leading edge of the main cloud band had passed eastward into Arkansas and Missouri. The trailing portions of the band are identified over southeastern Kansas and eastern Oklahoma. The region of clear skies had also progressed eastward into central Oklahoma and Kansas, while cirrus can be identified in the northwesterly flow over Colorado, western Kansas, and Oklahoma in association with the ridge-crest cirrus system identified earlier.

The broad characteristics of the cloud field that passed over Kansas and Oklahoma are strongly coupled to the synoptic-scale dynamics discussed above. During its passage through the analysis region, the cloud band existed *between* the wind speed gradient associated with the advancing jet streak and the diffluent trough axis to the east. The cloud band propagated eastward with these dynamical structures and maintained its overall orientation with them throughout the period. This correspondence can be understood by considering the horizontal divergence in the upper troposphere (Fig. 7). At 26/18, the cloud band can be seen to extend along the axis of horizontal divergence through central Oklahoma and Kansas. The placement of the horizontal divergence west of the trough axis and east of the speed gradient was discussed earlier. The coupling between the cloud and upper-tropospheric divergence remained strong at 27/00 (Fig. 6b) where the axis of horizontal divergence existed along the Kansas–Oklahoma border. At this time the maximum divergence had shifted north into eastern Kansas. Satellite imagery suggests the brightest clouds at 27/00 were north of the Kansas–Oklahoma border with dissipating cloud cover over eastern Oklahoma where upper-tropospheric divergence had decreased.

Of course, any correspondence of the cloud features with the horizontal divergence pattern in the upper troposphere follows directly from the vertical motions implied by mass continuity. Figure 14 shows a time sequence of kinematic vertical velocity cross sections that transect the cloud band along the Kansas–Oklahoma border. As expected, large-scale ascent is diagnosed in the middle and upper troposphere during this period. Broad gentle descent is also resolved in the lower stratosphere (the tropopause during this period was near 10.5 km). At 26/18, ascent is diagnosed between 2 and 8.5 km along the entire cross section with maximum vertical velocities of just over 3 cm s^{-1} occurring along 97.5°W—the approximate location of the cloud band identified in Fig. 5a. Values greater than 2 cm s^{-1} are estimated to extend to 7.5 km at this time. By 26/21, the vertical motion pattern along the cross section

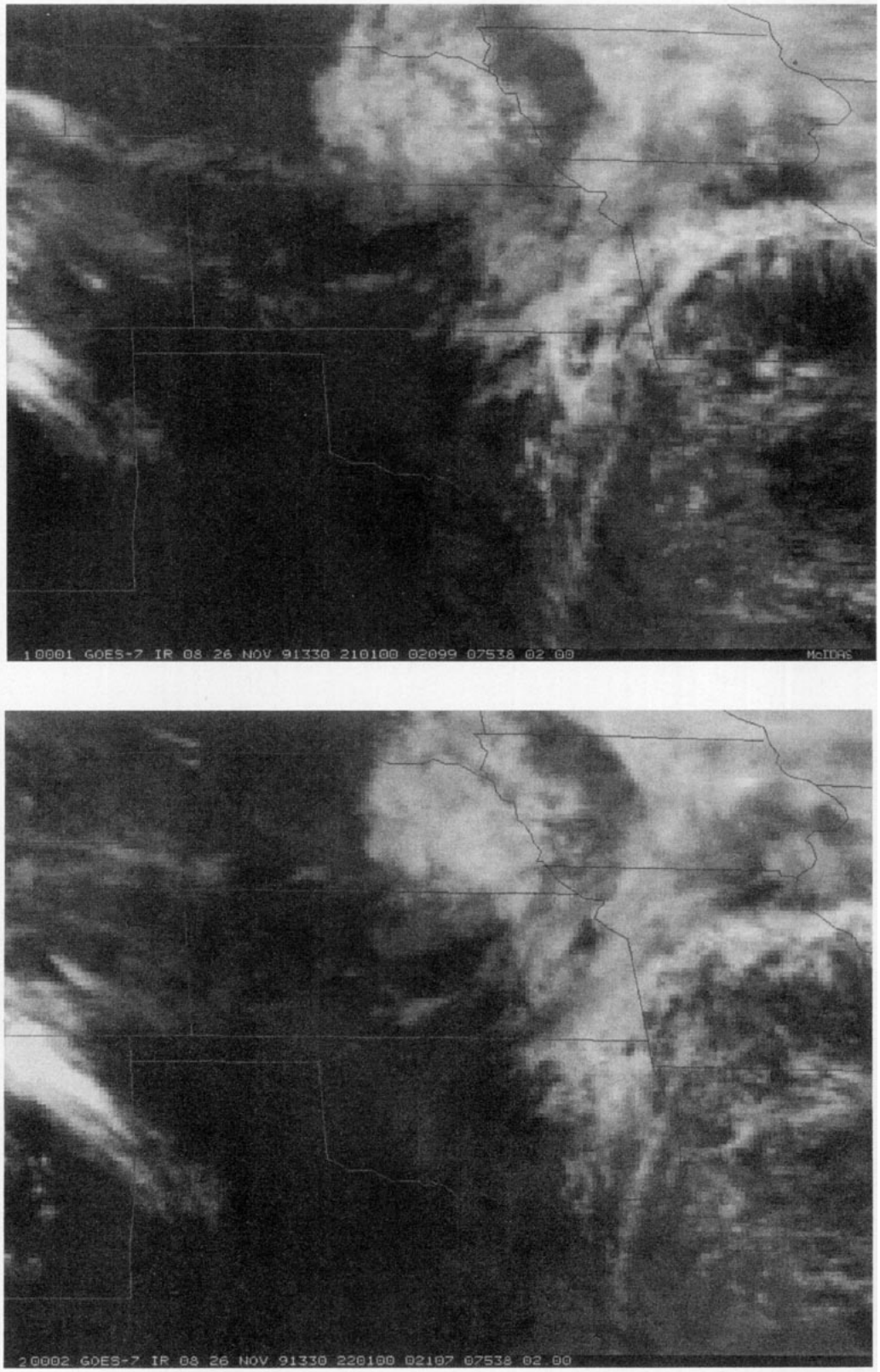

FIG. 13. *GOES-7* infrared imagery showing the progression of the middle- and upper-tropospheric cloud system through the Kansas–Oklahoma region at (a) 2100 UTC 26 Nov. 1991, (b) 2200 UTC 26 Nov. 1991, (c) 2300 UTC 26 Nov. 1991, and (d) 0000 UTC 27 Nov. 1991.

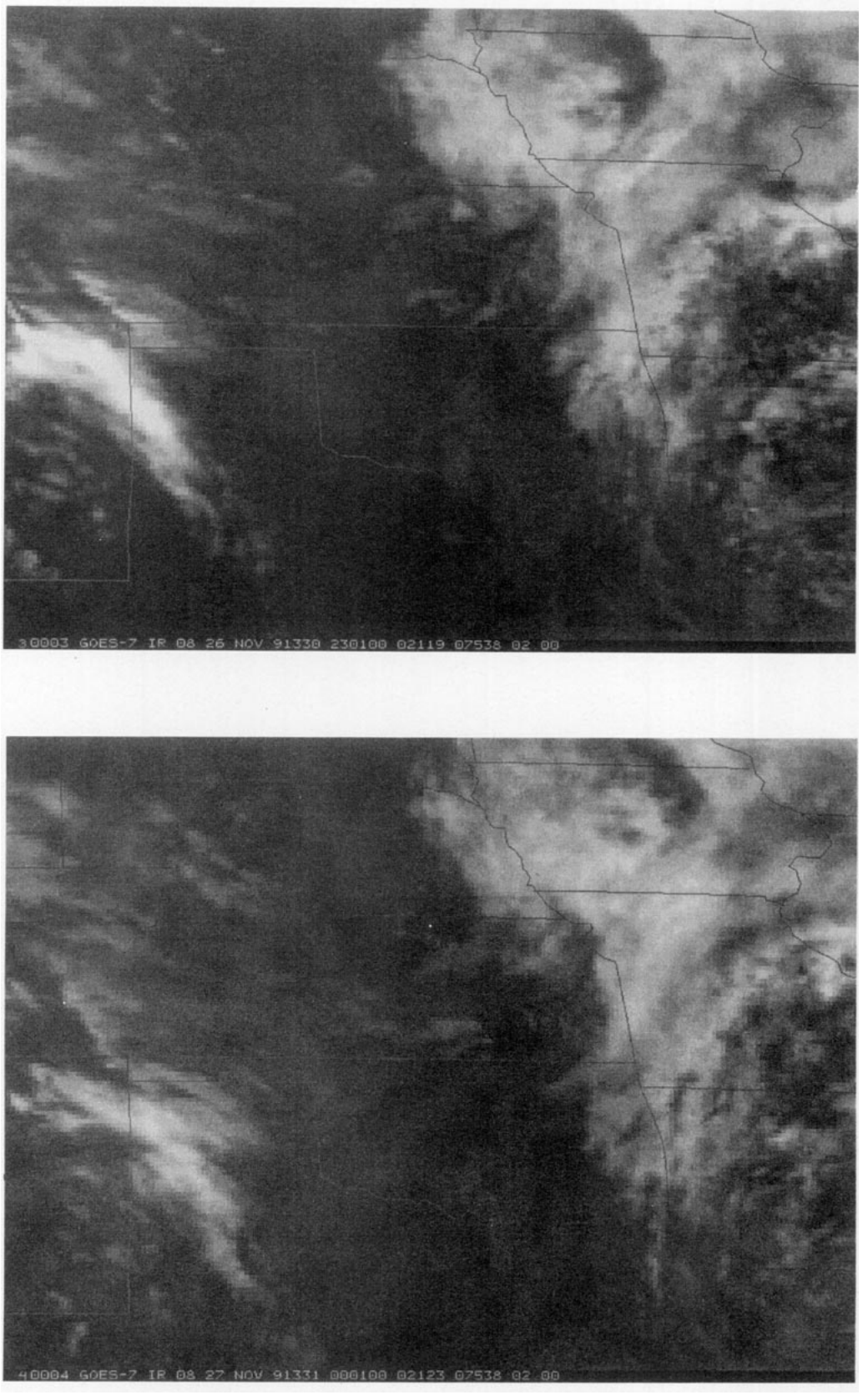

FIG. 13. (*Continued*)

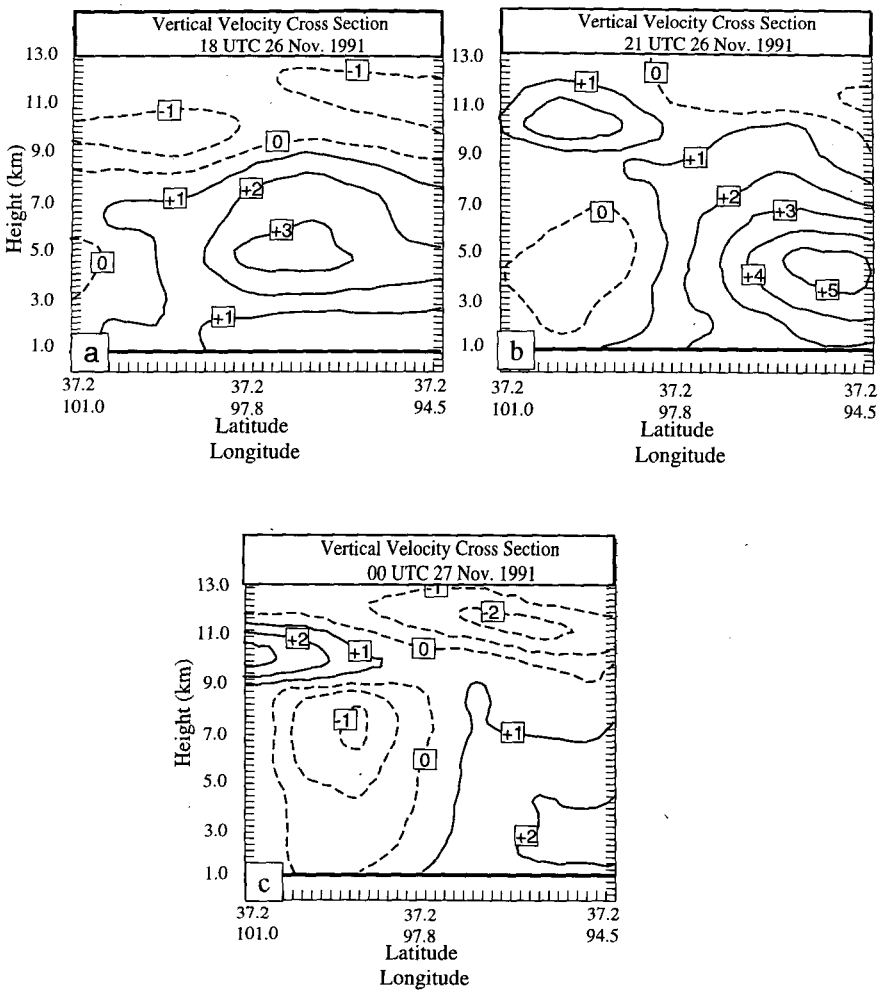

FIG. 14. Kinematic vertical velocity cross sections along the dashed line in Fig. 6. The cross sections are oriented such that the left side of the plot is the western end of the dashed line in Fig. 6. (a) 1800 UTC 26 Nov., (b) 2100 UTC 26 Nov., and (c) 0000 UTC 27 Nov. The contour interval is 1 cm s^{-1}, and negative values are contoured with dashed lines.

had shifted eastward and intensified significantly. Maximum ascent is still resolved near 4.5 km with peak values greater than 5 cm s^{-1} along 95°–96°W. Positive vertical motions are also resolved to a higher elevation at 26/21 with values greater than 2 cm s^{-1} occurring to 8 km and positive vertical motions suggested to 11 km. Recall that during this period active cirrus cloud formation was occurring in bands near the Kansas–Oklahoma border. These bands were propagating southeastward toward the leading edge of the main cloud formation. The cross section of vertical motions along the central portion of the main cloud shield at 26/21 is shown in Fig. 15. As before, peak upward motions are resolved in the middle troposphere near 37°N just south of the Kansas–Oklahoma border. The upper troposphere near this latitude is ascending, while upper-tropospheric subsidence is diagnosed north and south of the cirrus-generation area. Also, as suggested by imagery, the vertical motions throughout the troposphere decrease markedly in central and southern Oklahoma. By 27/00 (Fig. 14c), the region of maximum ascent had shifted eastward into southwest Missouri, and subsidence is resolved west of 98°W in all but a thin tropospheric layer between 9 and 12 km. The positive vertical motions are consistent with cirrus advancing into the western portion of the area in association with the approaching large-scale ridge crest cloud system. The trailing edge of the cloud band under consideration now existed over extreme eastern Kansas and Oklahoma.

Fortuitously, the hub of the FIRE Cirrus-II project at Coffeyville, Kansas (Fig. 1), was located very near the maximum large-scale vertical motions and most intense cirrus-generating region. This allowed extensive sampling of the characteristics of the clouds forced by the vertical motions described above. Figure 16 shows a

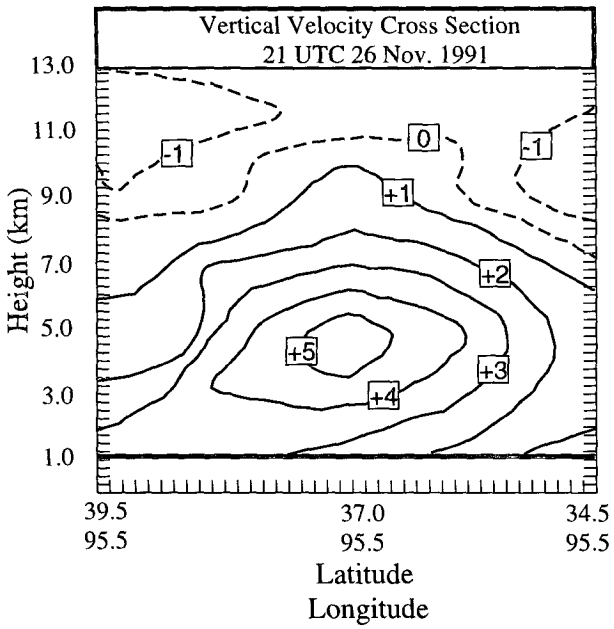

FIG. 15. Kinematic vertical velocity cross section along the dotted line in Fig. 6 at 2100 UTC 26 Nov. The cross section is oriented such that the left side of the plot is the northern end of the dotted line in Fig. 6. The plotting convention is as is Fig. 16.

time series of the data collected by the Pennsylvania State University 94-GHz cloud radar (Clothiaux et al. 1995) on the afternoon of 26 November. The leading edge of the cloud shield was first observed over Coffeyville at about 9 km. The layer of cirrus rapidly thickened after 1900 UTC, resulting in a cloud layer with a base at about 6.5 km and top ranging from 8.8 to 9.5 km. Aircraft reports indicate very thin cirrus extended up to about 10.5 km. The radar profile shows regions of enhanced power after 1915 UTC indicative of convective cells within the main cloud layer. Three organized precipitation streamers that penetrated below 6 km occurred between 1945 and 2115 as cloud base gradually lowered (Fig. 16). After 2115, a definite change in the character of the cloud was noted as cloud base lowered quite rapidly and returned power increased. By 2200 UTC cloud base was observed near 3 km. (Note that the radar minimum range was set at 3 km during this period, which precluded measurements below this height; cloud base did drop below 3 km as evidenced by ceilometer measurements.) Cloud top during this time was observed to decrease slightly to 8 km. The next major change in the cloud deck occurred after 2215 UTC. Cloud top and the upper extent of the region of enhanced reflectivity became more diffuse, and cloud top began to decrease rapidly, while the lower portions remained nearly unchanged. By 2330 UTC only scattered clouds were observed by the radar.

The local evolution of the vertical thermodynamic and moisture structure is of considerable importance when attempting to understand the coupling between the diagnosed dynamics and the observed local and regional cloud fields. We will consider the CLASS radiosonde soundings (see Fig. 1) recorded at Coffeyville, Iola (IOL), Arkansas City (ARK), and Muskogee (MUS) at 26/12, 26/15, 26/18, 26/21, and 27/00. Relative to Coffeyville, ARK is about 140 km to the west, IOL about 100 km to the north, and MUS about 160 km to the south. Also recall that the actual release times of the soundings are 30–45 minutes prior to the nominal sounding time and that the sondes reached 8 km about 25 minutes after launch. The time series of soundings for Coffeyville are shown in Fig. 17 where each successive sounding is offset by 10°C. Figure 18 shows time–height cross sections of relative humidity, and plotted in Fig. 19 are time series of potential temperature profiles.

The tropopause at Coffeyville was located at about 10.5 km (245 mb at −59.5°C) at 26/15 and slightly lower at 26/18 and 26/21 (Fig. 17). A much lower tropopause (9.4 km at 290 mb and −51.1°C) was observed at 27/00, although the region between 9.8 and 10.7 km does have a tropospheric lapse rate at this time with relative humidity with respect to ice (RHI) greater than 60%. Recall that this last sounding passed through the most vertically developed portion of the cirrus cloud band. Complex upper-tropospheric stability structure (multiple tropopause) is common in soundings taken in the vicinity of jet cores (e.g., Starr and Wylie 1990). The ARK soundings show a similar pattern with continued tropopause lowering and complex structure after the cloud band had passed, while IOL and MUS show less dramatic changes (Fig. 19). The general tendency is consistent with the diagnosed weakly subsident vertical motions in the lower stratosphere (Fig. 14).

The soundings generally exhibit a remarkable degree of thermal structure with a number of persistent and highly stable features (Fig. 19). Each location has a strong inversion at about the 2-km level that does not appear to change with time. Each also shows a second inversion that initially occurred at about the 3-km level (26/12) but subsequently lifted (especially after 26/18) before becoming fairly diffuse by 27/00 at Coffeyville and IOL where intense moistening and cloud development occurred below the 6-km level. By 27/00, this feature was located just below the 5-km level at ARK. Another less distinct but persistent stable feature was also initially observed just above the 6-km level at each site. This stable zone tended to lift weakly until 26/21 at Coffeyville and IOL followed by a dramatic rise. This feature has good correspondence with cloud base between 26/19 and 26/21 at Coffeyville and caps the region of very dry air below the region of initial cloud formation (Fig. 18). The observed vertical displacements of the midtropospheric stable features (and isentropes) is in very good agreement with the

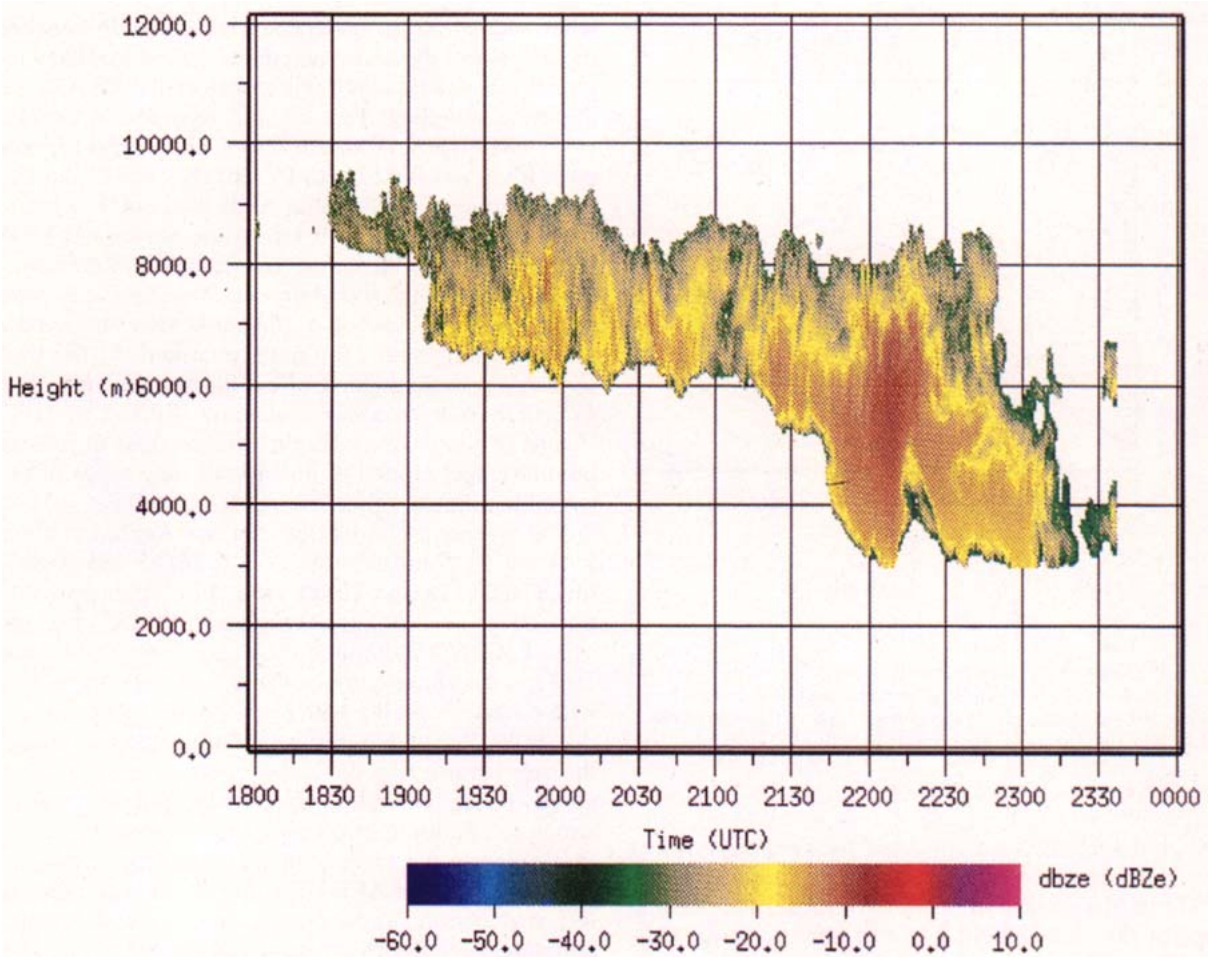

FIG. 16. Time–height cross section of reflectivities (dB*Ze*) observed by the Pennsylvania State University 94-GHz cloud radar from 1800 UTC 26 Nov. to 0000 UTC 27 Nov. 1991.

diagnosed pattern of vertical motion both temporally and spatially.

Warm air advection was observed at Coffeyville throughout the upper troposphere above 7 km in association with the progressive humidification of the region. However, strong cooling was observed between 26/21 and 27/00 (Fig. 19). Similar tendencies were observed at the other sites although differences are seen in the lower extent of the region of warm advection and in the timing of the changeover to cold advection. It is likely that the changeover from warm to cold advection roughly coincided with the dissipation of the upper portion of the cirrus band observed after 2245 at Coffeyville (Fig. 16), although this cannot be definitively established with the available data. The passage of the bright southwest–northeast cirrus band at IOL (Fig. 5b) also corresponds fairly well with the changeover there.

The thermal structure associated with this event showed a good deal of variability and complex development. The evolution of the moisture field as observed by the CLASS radiosondes is also quite interesting. The 26/15 and 26/18 soundings from Coffeyville (Fig. 17) show a layer of enhanced moisture (60% RHI or greater) at an altitude of 7 km with very dry air above and below this layer (Fig. 18). The 26/18 sounding was made in the cloud-free dry slot just ahead of the cloud band (Fig. 13). By 26/21, relative humidity exceeded 80% RHI in layers located at 7 and 8.8 km. The latter corresponds fairly well to the location of cirrus cloud top, while the former corresponds to the layer where cloud development was observed after 26/19 (Fig. 16). Later at 27/00, RHI exceeded 100% in the lower layer that had merged with the upper moist layer. Very strong moistening had occurred between 3 and 6 km in agreement with the radar cloud observations at 26/23 and the calculated vertical motion forcing (Fig. 12). Enhanced humidity is found up to nearly 11 km. This sounding passed through the cloud system at its most vertically developed stage (Fig. 16).

Soundings made to the north at IOL show similar moisture structure (Fig. 18) although the humidifica-

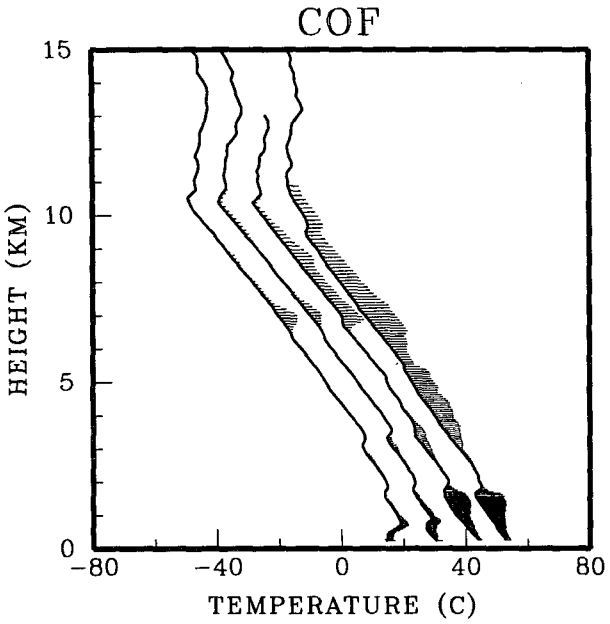

FIG. 17. Time series of temperature soundings at Coffeyville, Kansas, from 1500 UTC 26 Nov. 1991 to 0000 UTC 27 Nov. 1991. The profiles are each offset by 10°C with 1500 UTC on the left. Also depicted are the relative humidity profiles denoted by the shading extending to the right of each profile. The humidities are with respect to ice at temperatures below −20°C and with respect to liquid water at temperatures greater than 0°C. Between these temperatures the humidity is calculated as a linear combination of ice and liquid water. The shading begins at 40%.

tion above the 8-km level was observed earlier (26/15). This is consistent with the satellite imagery that indicates a much broader region of cirrus cloud development to the north of Coffeyville. The relative humidity patterns at Coffeyville and IOL are remarkably similar at lower levels. The evolution of the moisture field to the west at ARK shows a less intense pattern of moistening. The final 27/00 sounding at ARK was made in the clear region following the cloud band (Fig. 5c) and indicates substantial drying of the upper troposphere. Besides resolving the main cirrus deck between 6 and 9 km, the 26/21 ARK sounding also gives some indication of another layer of possible cloud formation near the 10-km level that is consistent with observations from one of the research aircraft (M. Poellot 1993, personal communication). It also appears that the downward extension of the cloud layer that was observed at Coffeyville after 26/2145 (Fig. 16) had probably not developed by the time the cloud band passed ARK. Soundings made to the south of MUS (Fig. 18) show elevated moist layers at higher altitudes (8 and 9.5 km) that were somewhat more distinct (e.g., at 26/21). As at ARK, the intense moistening below the 6-km level was not observed at MUS.

From our earlier discussions it is quite apparent that rather intense large-scale ascent existed over southeastern Kansas and northeastern Oklahoma as the synoptic-scale dynamics evolved during the afternoon of 26 November. Evidence for this ascent was also noted in the radiosonde time series discussed above. A time–height cross section of kinematically derived vertical motions using WPDN data and interpolated to Coffeyville is shown in Fig. 20. As expected, ascent is diagnosed below 8 km throughout the period, and vertical motions near zero are diagnosed at and above the tropopause. Peak ascent remains in the layer between 3 and 4 km. The vertical velocity in the cirrus generating region between 6 and 8 km and 26/19 and 26/21 is between 2 and 4 cm s^{-1}. At 26/22, when cloud base decreased to less than 3 km, maximum vertical velocities were near 7 cm s^{-1} at 3.5 km. After 26/23, the uplift decreases substantially throughout the troposphere, in reasonable correspondence with the change from warm to cold advection. This decrease in the vertical forcing also correlates well with the passage of the trailing edge of the main cloud band to the east of Coffeyville depicted on satellite imagery and in the radar time series.

Thus, the layer of initial cloud formation (7 to 9 km, Fig. 16) was a region of warm advection and progressive moistening in association with upward vertical motions. This region was bounded below by a stable frontal-like feature that progressively lifted. Two preexisting sublayers of enhanced moisture appear to have resulted in initial cloud generation at the 9-km level and then subsequent cloud generation at about the 7-km level in response to the continued forcing as well as possibly the moistening due to evaporation of ice crystals sedimenting from the higher layer. These two layers quickly merged. At 26/18, just prior to cloud formation, the thermal stratification in the layer from about 7 to 8 km was approximately neutral with respect to ice pseudoadiabatic processes, with distinct sublayers exhibiting conditional instability. By 26/21, this region of weak instability was located about 0.5 km higher in correspondence with the lifting of the bounding stable layer below. This corresponds well with the radar observations of cellular, that is, convective, development in the cloud layer and the initial visual observations of cirrus-generating cells. Layers of conditional instability were also observed at higher levels at 26/18; however, the general tendency was for progressive stabilization there, especially after 26/21.

The subsequent, rapid downward growth of the cloud layer after 26/2130 at Coffeyville was associated with a very rapid moistening of the layer between 3 km and the base of the existing cirrus clouds. This moistening likely resulted from quasi-horizontal advection but was also forced by the adiabatic cooling arising from the peak in upward motion in this layer and evaporation of falling ice crystals. The region between the two stable zones, approximately from 4 to 6 km at 26/18, was quite conditionally unstable. The stability structure became highly variable by 26/21 but still with evidence of good convective potential. Even at 27/00,

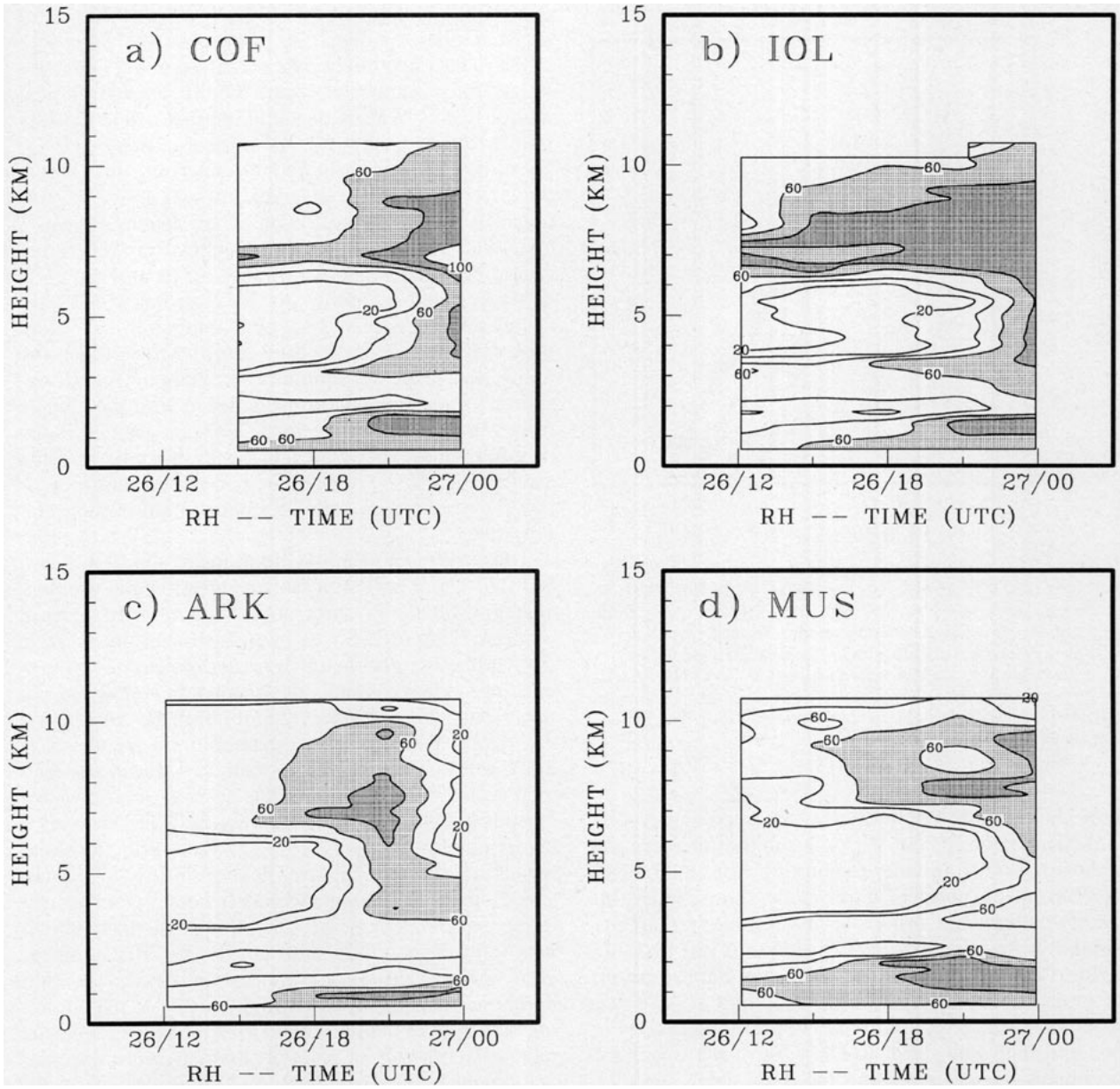

FIG. 18. Time–height cross sections of the relative humidity determined as in Fig. 19 from 1200 UTC 26 Nov. 1991 to 0000 UTC 27 Nov 1991 for (a) Coffeyville, Kansas, (b) Iola, Kansas, (c) Arkansas City, Oklahoma, and (d) Muskogee, Oklahoma. See Fig. 1 for the locations of these sites.

strong conditional instability was still observed between 3 and 4.5 km. The progressive lowering of the zone of conditional instability is consistent with the interpretation offered by Starr and Wylie (1990) based on the numerical simulations by Starr and Cox (1985a,b) where evaporation of falling ice crystals leads to downward propagation of a convective cloud generating layer through the combined effects of evaporative moistening and the destabilizing influence of associated evaporative cooling. In the present case we speculate that penetrative downdrafts could have developed in association with precipitation streamers falling into this conditionally unstable layer as relative humidity approached ice saturation and led to the rapid downward growth seen in Fig. 16.

4. Cirrus parameterization

The analyses presented in the preceding section have provided a time series of vertical velocity and relative

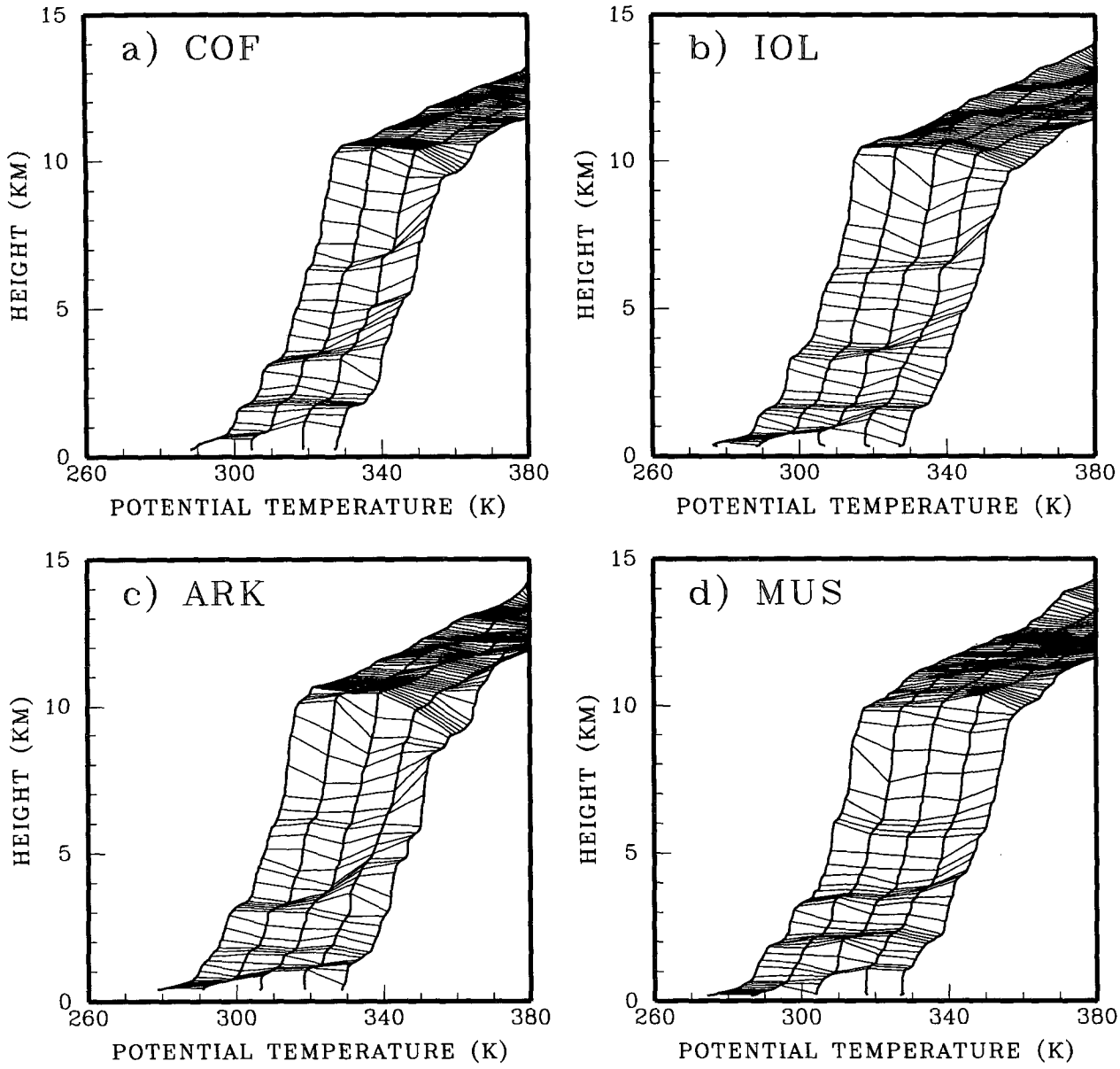

FIG. 19. Potential temperature profile time series beginning at 1200 UTC 26 Nov 1991 to 0000 UTC 27 Nov 1991 for (a) Coffeyville, Kansas, (b) Iola, Kansas, (c) Arkansas City, Oklahoma, and (d) Muskogee, Oklahoma. Each successive profile is offset by 10°C as in Fig. 19, and isentropes are drawn every 1 K.

humidity averaged over spatial scales of several hundred kilometers and centered on the FIRE Cirrus II operational hub at Coffeyville. We believe that these fields provide an accurate description of the synoptic-scale conditions at Coffeyville, unfiltered by any model assimilation. As such, these fields represent a purely data-based analog to the fields generated by GCMs. The two primary differences are that these data fields represent a directly observable atmospheric state (as opposed to GCM fields, which represent some particular realization of the model climatology) and their time resolution is somewhat coarser than that of a GCM. Given that these fields are analogous to GCM fields, they can be used to drive a cloud parameterization just as the parameterizations are driven in an actual model (Iacobellis and Sommerville 1989). Because observations of cloud properties were made during this period at the Coffeyville site, we have the unique opportunity to validate the clouds generated by the parameterization scheme. As an added benefit, our ability to simulate well the observed clouds can be used as a partial validation of the derived cloud fields.

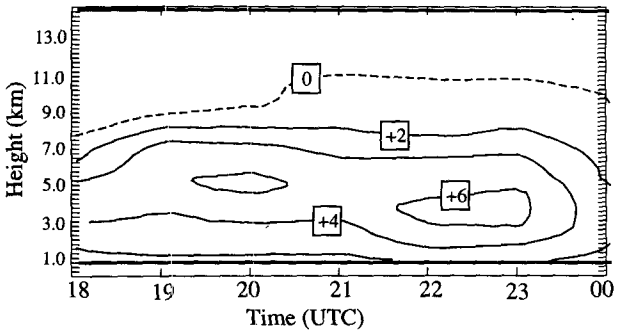

FIG. 20. Kinematic vertical velocity time–height cross section derived from the wind profiler horizontal divergence values interpolated to Coffeyville, Kansas. The plot is from 1800 UTC 26 Nov to 0000 UTC 27 Nov. The contour interval is 2 cm s^{-1}, and the zero contour is dashed.

To test this approach, we have used the HD parameterization (see section 1 for a brief description) forced by the vertical velocity field shown in Fig. 20 and the relative humidity with respect to ice observed by CLASS radiosondes at Coffeyville (Fig. 18). Vertical velocities were computed on the hour and are nominally valid during the 30 minutes before and after. The humidities, however, were recorded only at 26/18, 26/21, and 27/00 and were, therefore, linearly interpolated to the hours where no observations were available. The resulting bulk ice water contents are shown in Fig. 21 for the period 26/18 to 27/00. The temporal and vertical variability of this figure should be compared with the radar reflectivities for the same period (Fig. 16). The simulated cloud is well correlated with the observations in terms of bulk structure, although some differences are apparent. The parameterization captured quite well the early development of the cirrus and the subsequent deepening of the cloud. This latter occurs somewhat earlier in the parameterized cloud than was actually observed. This may be due to the spatial averaging of the wind field but is more likely due to the linear interpolation of the water vapor time series.

We have attempted to quantify one aspect of the parameterized cloud by comparing optical depths retrieved from sun photometer observations and those derived from visible satellite data (Minnis et al. 1993), with the optical depth parameterized from the ice water contents depicted in Fig. 21. To derive optical depths from the parameterized ice water contents, the temperature-dependent size distribution parameterization reported by Heymsfield and Platt (1984) is used in conjunction with the radiative parameterization of Ebert and Curry (1992). Since the parameterized cloud properties represent time-averaged quantities, the sun photometer data of Shiobara and Asano (1994) were averaged to 30-minute values. These data were also corrected for forward scattering of photons into the solar beam. The satellite optical depths are computed after the technique of Minnis et al. (1993) and represent spatially averaged (0.5 × 0.5 degree) data at a particular time. Table 1 shows the comparison. The parameterized and satellite-derived optical depths were temporally interpolated to the nominal valid times of the sun photometer data. Reasonable agreement is apparent early in the simulation with the three techniques reporting values less than or equal to two. At 1945 and 2019, the sun photometer and satellite techniques suggest thickening high clouds, while the simulation suggests thinning. By 2045, however, agreement between the parameterized and sun photometer is apparent, while the satellite-derived value changes little. However, the satellite-derived optical depth at 2045 is very uncertain due to increasing solar zenith angles. The discrepancies between the parameterized values and the observed quantities is maximized during the midpoint between soundings. In other words, agreement is good just after the 26/18 sounding and just before the 26/21 sounding. This indicates that 3-hour observations of the water vapor profile are not sufficient in this situation to resolve accurately the evolving moisture field. Comparisons for the entire period cannot be made because the sun photometer measurements are inaccurate at large optical thicknesses and low sun angles.

These simulation results are very encouraging from a number of perspectives. As shown theoretically by Starr and Cox (1985a,b) and observationally by Starr and Wylie (1990) and Sassen et al. (1989), the large-scale vertical velocity is a crucial component in the dynamical forcing of tropospheric cloud systems. The quality of this simulation suggests that our analysis scheme captured the essence of the vertical velocity field during this time period. Obviously, large-scale thermodynamical fields are also critical. Again, the good quality of the simulation, including particularly the optical depth comparisons, attests to the accuracy of our analysis. That the bulk characteristics of the cloud could be simulated adequately with synoptic-scale fields is encouraging from the point of view of GCMs since our fields contain information at comparable scales to GCMs.

This approach also demonstrates a clear path whereby cloud parameterizations can be improved. By using the observed fields, we have decoupled the parameterization problem from the model generation of forcing fields. Thus, the simulated clouds rely only on the accuracy of the analysis and the details of the parameterization and not on the model simulation (or assimilation) of the large-scale fields. While our approach has some drawbacks, most importantly the lack of availability of the data we require, it permits a quantifiable, iterative approach to the improvement of cloud parameterizations.

Finally, we should emphasize that this is only a single case. We have compared results from several other periods during the FIRE Cirrus II campaign, finding varying degrees of agreement with cloud radar and sat-

ellite observations. For the most part, significant disagreement was caused by a lack of accurate water vapor data in the upper troposphere. This was due to obvious failure of the humidity sensors at cold temperatures and to poor temporal resolution of the sonde launches. The analyzed vertical velocities were questionable in several instances.

5. Summary and conclusions

Field programs such as FIRE Cirrus II perform a valuable service to the scientific community by examining in great detail the evolution of cirrus clouds and associated radiative fields. Such a close examination provides a wealth of information from which generalizations can be made that ultimately influence the development of parameterizations. However, it can be stated unequivocally that one of the fundamental challenges to any attempt at improving cloud and radiation parameterizations in GCMs is how to actually couple the model atmosphere to the physical phenomena that are observed in the real atmosphere. This follows from the fact that the model's physical parameterizations are forced by the temporal and spatial scales of motion resolved by the model. *If the interaction between the scales represented by the GCM and that of the clouds is not thoroughly built into the parameterizations, increased knowledge of cloud microphysics and instantaneous radiation transfer through cirrus will not improve climate simulations.* Examining the connection between the evolving large-scale meteorology (that which is resolvable by GCMs) and the observed macroscale cloud properties has been the primary focus of this paper. We have concentrated on a 12-hour period

TABLE 1. Comparison between visible optical depths during the local afternoon of 26 Nov 1991. The values were determined using the cirrus parameterization described in the text: 30-minute averaged sun photometer data and satellite-observed visible data. See the text for further explanation.

26 Nov 1991 (UTC)	Parameterization	Sun photometer	Satellite
1845	1.7	1.2	1.1
1915	2.0	1.7	1.9
1945	1.5	3.5	2.8
2019	1.5	3.0	3.6
2045	1.9	1.5	3.4

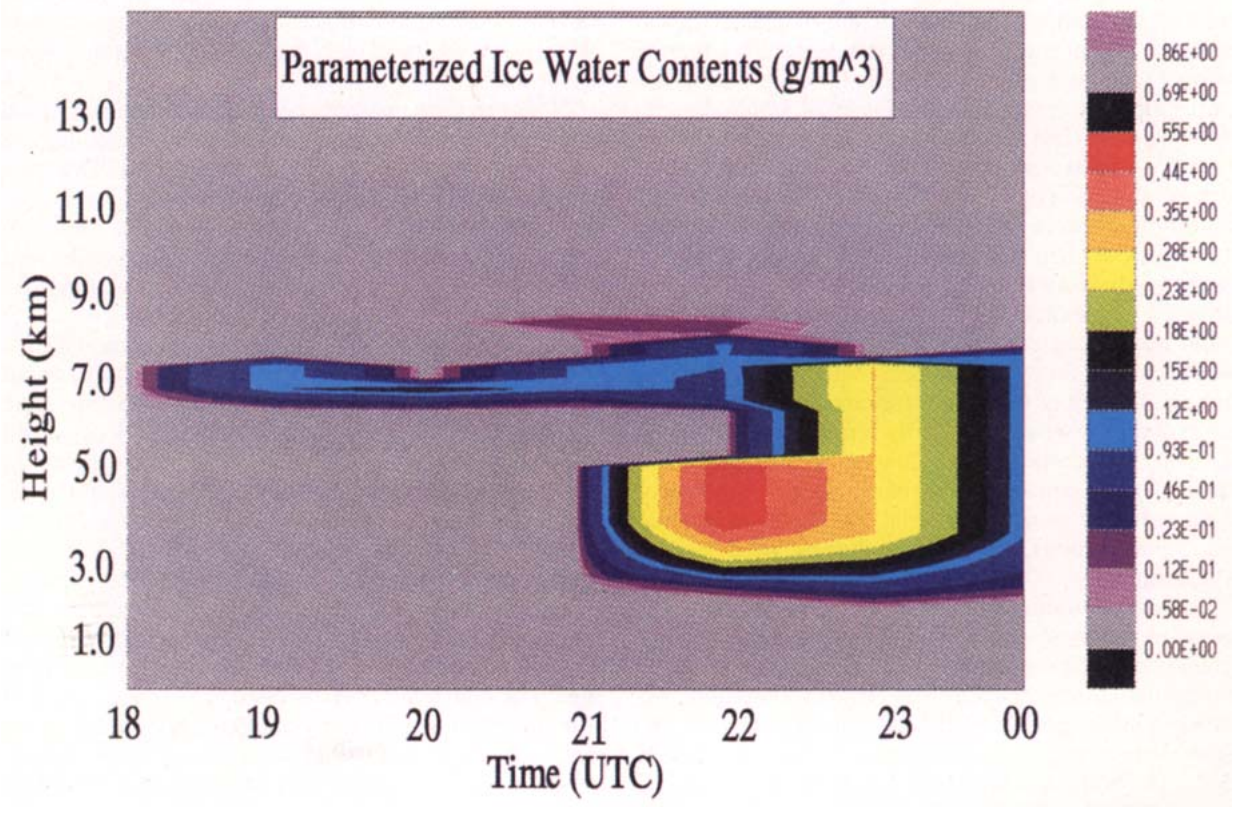

FIG. 21. Ice water content time–height cross section derived from the Heymsfield–Donner parameterization from 1800 UTC 26 Nov. to 0000 UTC 27 Nov. These values were determined by forcing the parameterization with the vertical velocities shown in Fig. 22 and the water vapor observed by radiosonde at Coffeyville (Fig. 20). No calculations were performed for temperatures above freezing, although the parameterization computes ice water contents at warmer temperatures due to precipitation from above.

from 1200 UTC 26 November 1991 to 0000 UTC 27 November 1991 during the field phase of FIRE Cirrus II held in Coffeyville, Kansas. The period we considered has become one of the focal cloud events of the field program.

We have utilized combined wind profiler and radiosonde data to generate the large-scale dynamical fields necessary for thorough analysis. Consistent with Thiebaux and Pedder (1987), Davies-Jones (1993), and Mace (1994), the analysis techniques were designed to minimize the uncertainty in the objectively analyzed quantities rather than to maximize the spatial resolution of the analysis product. As such, the analyses resolve synoptic-scale variability and approximate a 2 degree $\times$ 2 degree grid resolution of a typical GCM. Hourly kinematic analysis is possible using the time–space-converted (see appendix A) WPDN data. However, thermodynamic analyses are limited by the launch schedule of the radiosonde network.

A primary result of this study is the obvious coupling that has been demonstrated between the evolution of the synoptic-scale dynamics and the maintenance of a middle and upper tropospheric cloud band. Central to our argument is the indirect vertical circulation associated with the exit region of the strong jet streak that propagated into the western portions of the analysis region during the afternoon of 26 November 1991. The vertical circulation was found to be displaced to the cyclonic side of the jet, placing the descending branch below the jet axis and the ascending branch well to the left of the axis, just upstream of a small amplitude diffluent trough. The displacement of the circulation to the left of the axis was determined to have been caused by a combination of several factors. These included the amplifying diffluent trough and a building ridge in the southwestern United States. This juxtaposition of evolving dynamical features ensured that the along-stream ageostrophic flow was evolving with time and could not be neglected as is assumed in the development of the Sawyer–Eliassen equation. The geostrophic forcing of the transverse circulation was found to be due to a weakening of the cross-stream thermal contrast by geostrophic stretching deformation. The large-scale response to the weakening of the thermal contrast by the geostrophic wind was the frontogenetic transverse circulation. In this way thermal wind balance was maintained.

Embedded within the ascending branch of the indirect circulation was a middle and upper tropospheric cloud band. The orientation of the cloud band with the dynamical structures identified above was maintained throughout the period of the case study. Satellite imagery indicated active cirrus generation in thin bands along the Kansas–Oklahoma border between 26/20 and 26/23. This region of cloud formation correlated positively in both space and time with the maximum vertical motions in the ascending branch of the jet-induced circulation. These cloud features were sampled extensively by the FIRE Cirrus II field effort in southeastern Kansas and northeastern Oklahoma. The cloud band consisted of cirrus-generating cells early in the period (26/19–26/2130) and thickening middle-tropospheric cloud after 26/2145.

We demonstrated that an effective technique to verify the response of cloud parameterizations to GCM-scale dynamics is to decouple the parameterization from the model and force it with data. The output of the parameterization can then be verified against observations. Forcing the HD parameterization with kinematically derived vertical velocities (Fig. 20) and radiosonde-observed humidities (Fig. 18), we were able to show good correspondence between the temporal and vertical variability of the parameterized clouds (Fig. 21) and that observed by cloud radar (Fig. 16). Additionally, reasonable agreement was displayed between HD parameterized ice water paths and those retrieved from sun photometer observations.

The favorable comparison between the observations and parameterized clouds leads to several conclusions:

1) Cirrus cloudiness formed as part of a baroclinic leaf cloud structure can be successfully parameterized using a diagnostic cirrus parameterization and large-scale dynamics. It should be noted that, due to low horizontal wind speeds in the cirrus generation region, horizontal advection of ice over large distances was likely not a factor. Thus, the bulk diagnostic scheme performed well.

2) Given the sensitivity of the HD parameterization to the large-scale vertical velocity, we conclude that the diagnostic analyses generated from the WPDN data were of high enough quality to capture the essence of the vertical velocity field over Coffeyville. This also lends credence to the overall dynamical setting derived from the WPDN analysis of a jet-induced vertical circulation displaced poleward of the jet axis.

3) The technique used to test the HD parameterization is viable assuming adequate availability of input fields and of suitable verification data. The technique *requires* hourly wind profiler data from at least seven stations spread in an array about a central location. Thermal and moisture fields with at least 3-hour resolution are essential but may not always be sufficient. Hourly values derived from Radio Acoustic Sounding System and Raman lidar would be ideal and are necessary in highly variable situations. Verification of the parameterized quantities is difficult since the output of the parameterization scheme represents grid box averages. The conversion between the spatial and temporal domains made available by continuously operating remote sensors is a possible solution, although the retrieval of physical quantities from radar or lidar reflectivities is far from a solved problem. Verification of the area-averaged quantities using aircraft may be impossible owing to the very limited temporal and spatial sampling from these platforms as well as to the diffi-

culty of inferring fundamental quantities such as ice water content from the aircraft data.

While short-term intensive field campaigns like FIRE Cirrus II are absolutely essential for collecting in situ and remotely sensed cloud data for process studies, model development, and parameterization development, the points made above show the weakness of campaigns in terms of thorough testing and verification of GCM parameterizations. The Department of Energy's Atmospheric Radiation Measurement (ARM) program (Stokes and Schwartz 1994) is designed to address some of the shortcomings of campaign-style datasets. ARM has established a long-term observational facility known as the Southern Great Plains (SGP) Clouds and Radiation Testbed (CART) site within the inner array of the WPDN (Fig. 1). This facility will provide verification data needed for parameterization development and testing. The ARM program is essentially built around the concept known as single-column modeling (SCM) where all physical parameterizations are forced by observed dynamical fields. The forcing of the HD parameterization with these fields, which we presented in section 4, is a first step in the SCM concept. This type of approach, if properly implemented over a period of time containing many cloud events, will allow careful evaluation of parameterization performance, and improvements in GCM parameterizations will likely follow. However, the success of the SCM concept applied to the SGP CART site depends primarily on the quality and continuity of the input data. A primary component of the input data is observations from the inner array of the WPDN. No other observational platform can generate the temporal, vertical, and spatial consistency needed in the SCM concept. It can be stated with reasonable certainty that without a high quality and continuous data stream from the inner array of the WPDN and the CART instrumentation the data-based SCM approach envisioned by ARM will not succeed.

Our future work will be directed toward more quantitative verification of cirrus cloud parameterizations. Using the size distributions described by Heymsfield and Platt (1984) and the radiative parameterization of Ebert and Curry (1991), we are performing full radiative calculations based on the HD parameterization derived from the entire FIRE Cirrus II dataset. These results are being verified with surface-based observations and satellite-derived properties. These techniques, derived from the FIRE Cirrus-II period, are being further developed to operationally process the ARM SGP data stream. Current plans are to implement a full data-based single-column model (Iacobellis and Somerville 1989) and to apply this model to long time series of data.

Acknowledgments. We are indebted to Dr. Eugene Clothiaux and Dr. Bruce Albrecht for many useful and insightful discussions. We are grateful to Miss Laurie Bothell for assistance in preparing the manuscript and to Bill Smith and Andrew Lare for substantial help in preparing figures and acquiring data. This research was supported by the National Aeronautics and Space Administration (Grant NAG-1-1095) and by the U.S. Department of Energy (Grant DE-FG02-90ER61071).

APPENDIX A

Time–Space Conversion Technique

In the past the temporal resolution of observed tropospheric wind profiles was limited to the time required for a radiosonde to make an ascent from the surface to the tropopause. The finest temporal resolution possible tended to be about 2–3 hours. Also, due to the cost of operating temporally enhanced radiosonde networks, this resolution was only possible for short durations. A distinct advantage of wind profiler observations is the temporal continuity of the vertical profiles. To take advantage of the temporal continuity, an algorithm has been developed that converts the observed temporal characteristics of the wind into a spatial distribution of independent observations.

To preserve the integrity of the data, the time–space conversion (TSC) technique described here is limited in scope and is applied during a 3-hour period only when certain conditions are met. The period considered for the conversion extends from 1 hour before (denoted t_{-1}) to 1 hour after (t_{+1}) a current (t_0) observation. All three observations in time at a particular level must be present. The assumption is made that the winds along a curved trajectory streamline are subject only to the centripetal acceleration necessary to maintain the air parcels on the streamline. Additionally, it is assumed that the wind speeds vary linearly along the trajectory. With these assumptions, the approximation can be made that $V_{s_u}^{t} \approx V_{s_p}^{t+1}$ and $V_{s_d}^{t} \approx V_{s_p}^{t-1}$, where the superscripts refer to the time and the subscripts refer to a distance upstream (s_u), downstream (s_d), and at the profiler location (s_p). Therefore, the distances s_u and s_d are increments of arc appropriate for the location of the winds $V_{s_p}^{t+1}$ and $V_{s_p}^{t-1}$, respectively. These distances are estimated using forward and backward finite differencing to be

$$s_u = -\Delta t \frac{(V_s^{t_0} + V_s^{t+1})}{2}$$

$$s_d = \Delta t \frac{(V_s^{t_0} + V_s^{t-1})}{2}.$$

The endpoints of the streamline trajectories must be located in space. The schematic in Fig. A1 shows the geometry that is considered. It is assumed that the streamline defined by the three observations has a single radius of curvature: R_t is estimated by first mapping the WPDN observations at time t_0 to a Cartesian grid and then estimating the radius of streamline curvature

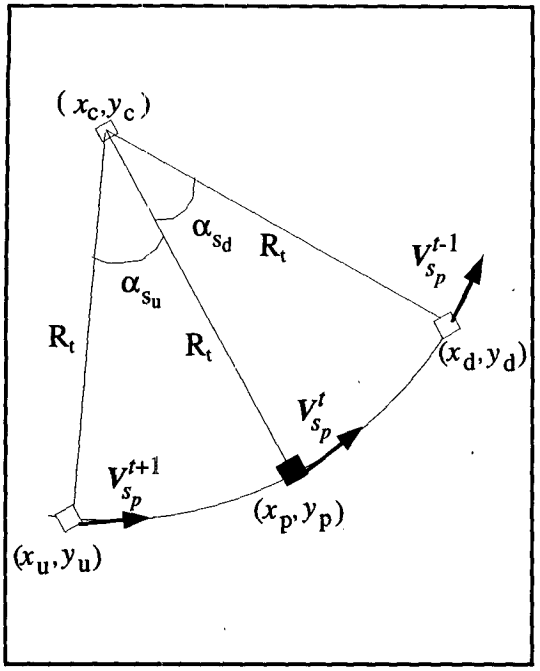

FIG. A1. The geometry considered in the time–space conversion algorithm discussed in appendix A.

R_s by incrementally stepping forward and backward along an arc of 100 km that is defined by the spatial distribution of wind observations. After determining R_s, R_t can be estimated using the equation (Holton 1979),

$$\frac{1}{R_t} = \frac{1}{R_s} + \frac{1}{V_{s_p}^{t_0}} \frac{\partial \beta}{\partial t},$$

where β is the observed wind direction at the profiler site and $\partial\beta/\partial t$ is estimated using centered differencing. Since the uncertainty in R_t increases with increasing curvature, the TSC algorithm does not continue if R_t is found to be less than 1000 km. The center of rotation of the parcel trajectory is then determined by noting that R_t is normal to the wind direction and to the left (right) of the flow for positive (negative) R_t. Therefore,

$$x_c = x_p - R_t \cos(\beta)$$

$$y_c = y_p - R_t \sin(\beta),$$

where x_c and y_c are the coordinate locations of the center of curvature and x_p and y_p are the coordinates of the profiler. The upstream and downstream locations are then estimated by noting that

$$\alpha_{s_u} = \frac{s_u}{R_t}$$

$$\alpha_{s_d} = \frac{s_d}{R_t},$$

where α_u and α_d are the angles subtended by the upstream and downstream locations with the radius of trajectory curvature. Therefore,

$$x_u = x_c + R_t \cos(\alpha_u + \beta)$$

$$y_u = y_c + R_t \sin(\alpha_u + \beta)$$

$$x_d = x_c + R_t \cos(\beta - \alpha_d)$$

$$y_d = y_c + R_t \sin(\beta - \alpha_d)$$

are the upstream and downstream locations assigned to the winds observed by the profiler at times t_{+1} and t_{-1} respectively.

APPENDIX B

Kinematic Vertical Velocities from Wind Profiler Data

The profile of vertical velocity can be determined by solving the continuity equation (Holton 1979)

$$\frac{\partial \rho}{\partial t} + (\nabla_h \cdot \rho \mathbf{V}_h) = -\frac{\partial}{\partial z}(\rho w), \qquad \text{(B1)}$$

assuming the vertical profile of horizontal divergence is known to good accuracy and appropriate boundary conditions are specified. In most previous applications of the kinematic method pressure was used as the vertical coordinate since the winds necessary to determine the horizontal divergence were acquired from radiosonde data. An exception to this is the work of Carlson (1989) and Hermes (1991). Since wind profilers measure the wind in physical height coordinates, no supplemental thermodynamic information is generally available that allows unambiguous mapping of the measured horizontal winds onto pressure surfaces. Therefore, in order to make the application of the kinematic method as general as possible, the continuity equation must be solved in a geometric height coordinate system.

Applying a vector identity to the mass flux convergence term on the right of Eq. (B1), using scale analysis for midlatitude synoptic-scale motion (Holton 1979), substituting for the air density from the ideal gas law in the second term on the left, dividing through by the air density, and solving for the vertical gradient of the vertical velocity from the three-dimensional velocity divergence, Eq. (B1) can be written

$$\frac{\partial w}{\partial z} = w\left(\frac{g}{RT} + \frac{1}{T}\frac{\partial T}{\partial z}\right) - (\nabla \cdot \mathbf{V}_h) - \frac{\partial \ln \rho}{\partial t}, \qquad \text{(B2)}$$

where all symbols take on their usual definitions and the subscript h is used to signify that only the horizontal components are considered. Equation (B2) is a first-order, linear nonhomogeneous differential equation that has a solution

$$w_{i+1} = \exp\left[-\int_{z_i}^{z_{i+1}} \frac{c_1}{T}\,dz\right] * \int_{z_i}^{z_{i+1}} \left(-\nabla\cdot\mathbf{V}_h - \frac{\partial \ln\rho}{\partial t}\right) \times \exp\left[-\int_{z_i}^{z} \frac{c_1}{T}\,dz'\right]dz + c*\exp\left[-\int_{z_i}^{z_{i+1}} \frac{c_1}{T}\,dz\right], \quad \text{(B3)}$$

where $c_1 = g/R + \partial T/\partial z$. The subscripts i and $i + 1$ represent discrete vertical levels and w_{i+1} is the vertical velocity at the vertical level $i + 1$ determined by solving the right-hand side using the vertical velocity w_i as a lower boundary condition. Equation (B3) can be simplified by bringing the first exponential term on the right within the leading integrand. The integral arguments of the exponential terms then subtract, changing the limits of integration in the argument of the exponential. The resulting expression can be written

$$w_{i+1} = \int_{z_i}^{z_{i+1}} \left(-\nabla\cdot\mathbf{V}_h - \frac{\partial \ln\rho}{\partial t}\right) \exp\left[\int_{z'}^{z_{i+1}} \frac{c_1}{T}\,dz'\right]dz + c*\exp\left[\int_{z_i}^{z_{i+1}} \frac{c_1}{T}\,dz'\right]. \quad \text{(B4)}$$

The solution of the equation for the vertical velocity at some level then depends on the vertical profile of horizontal divergence, the time rate of change of air density, and a boundary condition. For simplicity of notation the time rate of change of air density will be incorporated into the horizontal divergence in the remaining mathematical development, and the difference of the horizontal divergence and the local air density tendency will be denoted by the horizontal divergence. The boundary value c is the vertical velocity at the bottom or top of the vertical interval depending of the integration is performed upward or downward. The development here will assume an upward integration. Since the horizontal divergence and temperature are assumed known, this equation can be solved analytically by accounting for the vertical discretization of the data.

Following Hermes (1991), the assumption is made that the horizontal divergence varies linearly between data points according to the following equation:

$$\mathrm{div}g(z) = m_D z + B_D,$$

where m_D represents the slope of the divergence between data points and B_D is the intercept. It must be further assumed that the temperature in the layer being considered is isothermal with a value midway between the temperature at the top and bottom of the layer. In other words, the assumption is made that the vertical temperature profile is piecewise isothermal. The impact of these two assumptions will be discussed below. Applying the isothermal assumption to the temperature profile and evaluating the integrals to the exponential arguments, Eq. (B4) becomes

$$w_{i+1} = -\exp\left\{\frac{c_1}{T_0} z_{i+1}\right\} \int_{z_i}^{z_{i+1}} (\nabla\cdot\mathbf{V}_h) \exp\left\{-z\frac{c_1}{T_0}\right\}dz + w_i * \exp\left\{-\frac{c_1}{T_0}\Delta z\right\}.$$

Invoking the piecewise linear assumption to the horizontal divergence, we can write

$$w_{i+1} = -\exp\left[-\frac{c_1}{T_0} z_{i+1}\right]\left\{m_D \int_{z_i}^{z_{i+1}} z \exp\left[-z\frac{c_1}{T_0}\right]dz + B_D \int_{z_i}^{z_{i+1}} \exp\left[-z\frac{c_1}{T_0}\right]dz\right\} + w_i \exp\left[-\frac{c_1}{T_0}\Delta z\right].$$

The two resulting integral terms on the right can now be evaluated analytically,

$$w_{i+1} = -\frac{\exp\left[-\frac{c_1}{T_0} z_{i+1}\right] T_0}{c_1} \times \left(m_D\left\{\exp\left[-\frac{c_1}{T_0} z\right]\left(z - \frac{T_0}{c_1}\right)\right\}_{z_i}^{z_{i+1}} + B_D\left\{\exp\left[-\frac{c_1}{T_0} z\right]\right\}_{z_i}^{z_{i+1}}\right) + w_i * \exp\left[-\frac{c_1}{T_0}\Delta z\right]. \quad \text{(B5)}$$

The sensitivity of Eq. (B5) to the assumptions imposed on the profiles of temperature and horizontal divergence was examined with several analytical functions. The sensitivity to the assumption imposed on the temperature profile was found to be negligible in all cases. The difference in the vertical velocities derived with an analytical divergence profile and a discrete version of the profile reached a maximum of 0.5 cm s^{-1} only when a single convergence–divergence couplet existed in the vertical column.

A further limitation to the accuracy of Eq. (B5) when applied to wind profiler network data is the specification of an appropriate lower boundary condition. Since the lowest data level occurs near 500 m above the local ground level with the WPDN data, a significant portion of the near-surface layer is not sampled. Therefore, the most obvious boundary condition, that the vertical velocity at the surface is zero, becomes somewhat more difficult to impose. Hermes (1991) estimated the vertical velocity across the lower data boundary using estimates from a radiosonde network. Carlson (1989) reasoned that the vertical motions in

the lower stratosphere are typically small in a mass-weighted sense and solved the continuity equation from the top of the column to the lowest level. Since the data column observed by the WPDN wind profilers begins near 500 m above ground level (the Hermes data ended at 2.3 km, while the Carlson's and Forbes data ended near 1 km), the horizontal divergence is linearly extrapolated from the lowest data layers to the surface where the vertical velocity is known to be zero. The influence of sloping terrain is ignored due to the low relief typical of the analysis region.

As noted by numerous investigators (O'Brien 1970; Holton 1979; Carlson 1989; Starr and Wiley 1990), errors in the horizontal divergence at a particular level tend to be communicated to all higher levels. This results in large uncertainties in the calculated vertical motions. Therefore, the technique described by O'Brien (1970) is applied. This procedure adjusts the profile of horizontal divergence so that the vertical motion is forced to obey a specified upper boundary condition. Since the WPDN data generally reaches the lower stratosphere, an upper condition of $w = 0$ is imposed. Using random error generally expected from objectively analyzed wind profiler and radiosonde data ($\leq 2.5 \times 10^{-5}$ s^{-1}), it was found that the rms uncertainty in the kinematic vertical velocity when adjusted by the O'Brien technique was on the order of 2 cm s^{-1}.

REFERENCES

Ackerman, T. P., K. N. Liou, F. P. Valero, and L. Pfister, 1988: Heating rates in tropical anvils. *J. Atmos. Sci.*, **45,** 1606–1623.

Akima, H., 1978: A method of bivariate interpolation and smooth surface fitting for values given at irregularly distributed points. *ACM-TOMS*, **4,** 160–164.

——, 1984: On estimating partial derivatives for bivariate interpolation of scattered data. *Rocky Mtn. J. Math.*, **14,** 41–52.

Cammas, J., and D. Ramond, 1989: Analysis and diagnosis of the composition of ageostrophic circulations in jet–front systems. *Mon. Wea. Rev.*, **117,** 2447–2462.

Carlson, C. A., 1989: Kinematic quantities derived from a triangle of VHF Doppler wind profilers. M.S. thesis, Dept. of Meteorology, The Pennsylvania State University, 136 pp.

Chadwick, R. B., 1986: Wind profiler demonstration system. *Handbook of MAP*, Vol. 20, URSI/SCOPTEP, 336–337.

Clothiaux, E. E., M. A. Miller, B. A. Albrecht, T. P. Ackerman, J. Verlinde, D. M. Babb, R. M. Peters, and W. J. Syrett, 1995: An evaluation of a 94-GHz radar for remote sensing of cloud properties. *J. Atmos. Oceanic Technol.*, **12,** 201–229.

Conover, J., 1960: Cirrus patterns and related air motions near the jet stream as derived by photography. *J. Meteor.*, **17,** 532–546.

Davies-Jones, R., 1993: Useful formulas for computing divergence, vorticity, and their error from three or more stations. *Mon. Wea. Rev.*, **121,** 713–725.

Ebert, E. E., and J. A. Curry, 1992: A parameterization of ice cloud optical properties for climate models. *J. Geophys. Res.*, **97,** 3831–3836.

FIRE Project Office, 1991: FIRE Cirrus Intensive Field Observations II: Operations Plan. 113 pp. [Available from FIRE Project Office, MS 483, NASA Langley Research Center, Hampton, VA 23665-5225.]

Fischler, M. A., and R. C. Bolles, 1981: Random sample consensus: A paradigm for model fitting with applications to image and automated cartography. *Commun. Assoc. Comput. Mach.*, **24,** 381–395.

Frankhauser, J. C., 1969: Convective processes resolved by a mesoscale rawinsonde network. *J. Appl. Meteor.*, **8,** 778–798.

Gage, K. S., and B. B. Balsley, 1978: Doppler radar probing of the clear atmosphere. *Bull. Amer. Meteor. Soc.*, **59,** 1074–1092.

Hermes, L. G., 1991: Comparisons of rawinsonde-deduced kinematic and thermodynamic quantities with those deduced from VHF profiler observations. *Mon. Wea. Rev.*, **119,** 1693–1712.

Heymsfield, A. J., 1977: Precipitation development in stratiform ice clouds: A microphysical and dynamical study. *J. Atmos. Sci.*, **34,** 367–381.

——, and C. M. R. Platt, 1984: A parameterization of the particle size spectrum of ice clouds in terms of the ambient temperature and the ice water content. *J. Atmos. Sci.*, **41,** 486–855.

——, and L. J. Donner, 1990: A scheme for parameterizing ice-cloud water content in general circulation models. *J. Atmos. Sci.*, **47,** 1865–1877.

Holton, J. R., 1979: *An Introduction to Dynamic Meteorology*. Academic Press, 391 pp.

Iacobellis, S. F., II, and R. C. J. Sommerville, 1991: Diagnostic modeling of the Indian monsoon onset. Part I: Model description and validation. *J. Atmos. Sci.*, **48,** 1948–1959.

Keyser, D., and M. A. Shapiro, 1986: A review of the structure and dynamics of upper-level frontal zones. *Mon. Wea. Rev.*, **114,** 452–499.

Liou, K. N., 1986: Influence of cirrus clouds on weather and climate: A global perspective. *Mon. Wea. Rev.*, **114,** 1167–1199.

Mace, G. G., 1994: Development of large-scale diagnostic analysis techniques applicable to regional arrays of wind profilers and radiosondes. Ph.D. dissertation, The Pennsylvania State University, 261 pp.

Minnis, P., K. Liou, and Y. Takano, 1993: Inference of cirrus cloud properties using satellite-observed visible and infrared radiances. Part I: Parameterization of radiance fields. *J. Atmos. Sci.*, **50,** 1279–1304.

O'Brien, J. J., 1970: Alternate solutions to the classical vertical velocity problem. *J. Appl. Meteor.*, **9,** 197–203.

Sanders, F., L. F. Bosart, and C.-C. Lai, 1991: Initiation and evolution of an intense upper-level front. *Mon. Wea. Rev.*, **119,** 1337–1367.

Sassen, K., D. O'C. Starr, and T. Uttal, 1989: Mesoscale and microscale structure of cirrus clouds: Three case studies. *J. Atmos. Sci.*, **46,** 371–396.

——, D. O'C. Starr, G. G. Mace, M. R. Poellot, S. J. Melfi, W. L. Eberhard, J. D. Spinhirne, E. W. Eloranta, D. E. Hagen, and J. Hallet, 1994: The 5–6 December 1991 FIRE IFO II jet stream cirrus case study: The influence of volcanic aerosol. *J. Atmos. Sci.*, **51,** 97–123.

Shapiro, M. A., 1978: Further evidence of the mesoscale and turbulent structure of upper level jet stream-frontal zone systems. *Mon. Wea. Rev.*, **106,** 1100–1111.

——, 1981: Frontogenesis and geostrophically forced secondary circulations in the vicinity of jet stream-frontal systems. *J. Atmos. Sci.*, **38,** 954–973.

Shiobara, M., and S. Asano, 1994: Estimation of cirrus optical thickness from sun photometer measurements. *J. Appl. Meteor.*, **33,** 672–681.

Slingo, J. M., 1987: The development and verification of a cloud prediciton scheme for the ECMWF model. *Quart. J. Roy. Meteor. Soc.*, **113,** 899–927.

Soden, B. J., and L. J. Donner, 1994: Evaluation of a GCM cirrus parameterization using satellite observations. *J. Geophys. Res.*, **99,** 14 401–14 413.

Starr, D. O'C., and S. K. Cox, 1980: Characteristics of middle and upper tropospheric clouds as deduced from rawinsonde data. Colorado State University Atmos. Sci. Paper No. 327, 71 pp.

——, and S. K. Cox, 1985a: Cirrus clouds. Part I: A cirrus cloud model. *J. Atmos. Sci.*, **42,** 2663–2681.

——, and ——, 1985b: Cirrus clouds. Part II: Numerical experiments on the formation and maintenance of cirrus. *J. Atmos. Sci.*, **42,** 2663–2681.

——, and D. P. Wylie, 1990: The 27–28 October 1986 FIRE cirrus case study: Meteorology and clouds. *Mon. Wea. Rev.*, **118,** 2259–2287.

——, and S. H. Melfi, 1991: The role of water vapor in climate: A strategic plan for the GEWEX Water Vapor Project (GVaP). NASA Conf. Publ. CP-3120, 50 pp. [Available from International GEWEX Project Office, Washington, D.C.]

Stone, R. G., 1957: A Compendium on Cirrus and Cirrus Forecasting. Air Weather Service Tech Rep. AWS/TR 105-130, 80 pp. [Available from Air Weather Service, Scott AFB, IL, 62225.]

Strauch, R. G., B. L. Weber, A. S. Frisch, C. J. Little, D. A. Merritt, K. P. Moran, and D. C. Welsh, 1987: The precision and relative accuracy of profiler wind measurements. *J. Atmos. Oceanic Technol.*, **4,** 563–571.

Thiebaux, H. J., and M. A. Pedder, 1987: *Spatial Objective Analysis, with Applications in Atmospheric Science.* Academic Press, 299 pp.

Weldon, R., 1979: Cloud patterns and the upper tropospheric wind field. Air Weather Service Tech Rep. AWS/TR-79/003, 80 pp. [Available from Air Weather Service, Scott AFB, IL, 62225.]

Zamora, R. F., M. A. Shapiro, and C. A. Doswell III, 1987: The diagnosis of upper tropospheric divergence and ageostrophic wind using profiler wind observations. *Mon. Wea. Rev.*, **115,** 871–884.